Computational Fluid Dynamics (CFD) To Simulate Slug Flow in Horizontal Pipeline and Annular Pipe

by

Hassn Hadia

A thesis submitted to the School of Graduate Studies in partial fulfillment of the requirements for

The degree of

Masters of Engineering

Faculty of Engineering and Applied Science

Memorial University of Newfoundland

May, 2018

St. John's Newfoundland

Abstract

Slug flow can emerge as a factor in several industrial processes, especially in the oil and gas (O&G) industry. However, because of the complications that are inherent in multiphase flow, finding or developing a viable analysis tool has thus far proven elusive. For the past few decades, computational fluid dynamics (CFD) has served as the preferred approach in the flow analysis of single phase flow, yet it is only now beginning to be used in multiphase flow. Therefore, if CFD is to be adopted on a larger scale in the (O&G) industry, it is imperative that we first explore the wide variety of models currently existing in the commercial realm.

This thesis investigates the commercial CFD package ANSYS 16.2 analysis of (air-water slug flow) and (water-sand slurry flow) inside a horizontal pipe (2-15 m long with a 0.05-0.059 m internal diameter) and an annular pipe (2- 4.5 m long, 0.02- 0.088 m inner and 0.04-0.12 m outer diameter). A range of two-phase air/water flow simulations is carried out using the Eulerian model with the Reynolds Stress Model (RSM), and the volume of fluid (VOF) model with the Shear-Stress-Transport (SST) model option of turbulence. The aim is to simulate a range of fluid velocities between 1.66 and 7 m/s and a range of gas velocities between 0.55 and 11 m/s. Additional investigations include comparing CFD predictions along with experimental measurements in the literature and performing sensitivity studies.

In the present work, the impact from fluid-structure interaction (FSI) is demonstrated by using a 2-way coupling in ANSYS, effectively joining CFD and structural analysis. At the same time, stress and pressure changes are measured, along with the deformational structural response arising from unsteady multiphase flow. It is hoped that the outcome of this study will assist engineers and

researchers in making better decisions in terms of operation, design, and sizing of two-phase flow systems, as these systems have broad and promising applications in subsea (O&G) pipelines.

Acknowledgments.

First of all, I wish to thank my supervisor, Dr. John Shirokoff, along with my co-supervisor, Dr. Aziz Rahman, whose advice and encouragement guided me into the field of O&G research. Both have had an enormous impact not only on my future career options but also on my life. Under your direction, I discovered the fascinating depths of CFD multi-phase slug flow in pipes. Also gave me the necessary technical support. Without your help, I would not have been able to bring my research to a successful conclusion, and for that I will be thankful to you for the rest of my life.

As well, I extend my gratitude to Mr. Rasel Sultan. Your ongoing encouragement, together with your deep knowledge and technical support, were crucial in helping me create my model.

I also extend my thanks to the Libyan Ministry of Higher Education through the Canadian Bureau for International Education (CBIE). Without their financial assistance, this work would not have proceeded, and for that I am deeply grateful.

Last but not least, I wish to thank my parents and my family for their ongoing encouragement during the time at Memorial University, and for their life-long love and support, and my wife and children – thank you so much for everything you do for me. My wife has helped make these past two years not only endurable but happy.

Table of Contents

List of Tables

List of figures

Nomenclature

Name	Symbol
Density	ρ
Instantaneous velocity	u
Pressure	p
Viscous stress tensor	τ
Gravity vector	$\vec{g}$
Mass Weighted	F_{avre}
Flow quantity	f
Mass transfer from the p^{th} to the q^{th} phase	$\dot{m}_{pq}$
Mass transfer from the q^{th} to the p^{th}phase	$\dot{m}_{qp}$
Phase reference or volume averaged density of the q^{th}phase	ρ_{rq}
Viscosity	μ
Velocity	v
Force term	$\vec{F}$
Interface between the two phases	S
Physical density of one phase (q)	ρ_q
Generation of turbulence kinetic energy due to mean velocity gradients	G_k
Generation of ω	G_w
Effective diffusivity of k	T_k
Effective diffusivity of ω	T_w
Dissipation of k due to turbulence	Y_k
Dissipation of ω due to turbulence	Y_w

User-defined source terms	S_K and S_w
Turbulent Prandtl numbers for k	σ_k
Turbulent Prandtl numbers for ω	σ_w
Turbulent viscosity	μ_t
Average rate-of-rotation tensor	Ω_{ij}
Coefficient damps	α^*
Turbulent viscosity for blending functions	F_1 and F_2
Distance to subsequent surfaces	y
Positive component in the cross-diffusion term	D_w^+
Turbulence kinetic energy production	G_k
ω production	G_w
Turbulence kinetic energy dissipation	Y_k
Dissipation of ω	Y_w
Constant flexural rigidity	EI
Pipe's internal area	A
Pipe length	L
Pipe radius	R
Normalized radial setting for pipe, r	R/r
Gas velocity	V_g, V_{air}
Liquid velocity	V_l, V_{water}
Time in seconds	t
Distance between inner and outer wall of the annular pipe	y/ξ

Chapter 1

1.1 Introduction

When gas and water move along a pipeline at the same time, differences in density can cause the two phases to distribute in several different configurations. In general, operating conditions (e.g., pipeline angle and phase velocities) determine the phase distribution in pipelines [1]. One type of flow is “slug flow”, which is unstable and complicated. Despite the rate of liquid and gas flow staying more or less the same, extreme variations in time can appear in pipeline cross-sections, phase velocities and pressure, and component mass flow rates. This leads to the destabilization of heat and mass transfer processes. At the same time, the interruptions in flow due to slug flow can lead to vibration and pressure drops throughout the length of the pipe, potentially causing damage to pipe supports and bend as well as pipe corrosion (if there is sand in the flow). Slug flow can also detrimentally affect equipment used for the separation process. In this case, slug catchers, which are a type of pre-separation vessel, must be used to collect the slugs, which can occur in numerous industrial processes, including those related to oil and gas because such large supplies of oil and gas are used globally every day, even a minor improvement in the efficiency of the extraction process would have a major effect on overall industry costs. The key here is to source the appropriate analysis tools that will aid in optimizing multiphase flows for oil and gas companies [2].

Computational fluid dynamics (CFD), which was developed and has been used over the past 70 years, is an analysis tool commonly applied to subsea equipment. In the 1990s, CFD was used for single-phase flow calculations, which were made easier by the introduction of commercially

available CFD software like ANSYS Fluent Utilizing CFD for slug flow is, at the time of writing this thesis, still relatively rare, but given the ramp-up in computer resources that is rendering complex analyses not only possible but simple, CFD is becoming increasingly better known in this area [3]. The inclusion of slug flow models within the commercial mentioned above is assisting in the popularization.

Error sources persist in some of the simulations, which is to be expected. However, usage errors can be problematic. Misapplication of models, along with inaccurate parameters and boundary conditions can cause severely skewed results. Therefore, considering the preference for using CFD simulations in engineering projects, it is imperative to gauge the correctness and aptness of commercial codes, along with the types of models chosen. This can be especially crucial in slug flow situations, where complicated physical laws and numerical treatment renders the correct choice of appropriate models not readily apparent [4].

To date, very little investigation has been made into comparing commercial CFD codes. These codes and models can be created and applied to specific multiphase area, but codes that are well-suited to one type of commercial area might not be applicable to another. Given the need for specificity, it might be necessary and indeed useful to compare all available models, with the aim of building a knowledge base for slug flow simulations that utilize commercial-grade software [5].

1.2 Objective

In this thesis, the main objective is to use numerical simulations and validation in relation to experimental data as a means to lay a knowledge foundation suitable for defining multi-phase slug flow CFD processes. To that end, a two range of multi-phase models on ANSYS CFD software is

investigated in order to determine their suitability (i.e., their benefits as well as their limitations) in slug flow applications. Additionally, the aim is to formulate a CFD model that will not only be viable but also useful in general research into pipelines and/or annular pipe flows in relation to multi-phase slug fluids. Finally, we aim to determine the validity of our proposed model when applied in two-phase air-water slug flow in a pipeline, as well as to explain Fluid-Structure Interaction (FSI).

1.3 Organization of the Thesis

This thesis is written in manuscript format. Outline of each chapter is explained below:

Chapter 1 is a brief introduction of CFD slug flow in pipes with the ANSYS software.

Chapter 2 presents a Computational Fluid Dynamics Study of Two-Phase Slurry and Slug Flow in Horizontal Pipelines.

Chapter 3 presents Analyses of Slug flow Through Annular Pipe.

Chapter 4 is the overall conclusion of the study and further potential research scope in this area.

Chapter 2

A Computational Fluid Dynamics Study of Two-Phase Slurry and Slug Flow in Horizontal Pipelines

Hassn Hadia[1*], Rasel Sultan[1], Mohamed Rahman[2,] John Shirokoff[1], Sohrab Zendehboudi[1]

[1]Faculty of Engineering and Applied Science, Memorial University of Newfoundland, Canada
[2] Faculty of Petroleum Engineering, Texas A&M University at Qatar, Doha, Qatar

Abstract

This paper presents a Computational Fluid Dynamics (CFD) model to simulate two-phase slurry (water/sand) and slug (water/air) flow systems through utilizing the ANSYS Fluent simulation package. The CFD model is used to forecast the start and growth of the slug phase as well as its effect on horizontal vibrations. Eulerian model with Reynolds Stress Model (RSM) turbulence closure is considered to numerically analyze the slug and slurry flow of mono-dispersed fine particles at high concentrations. The Eulerian model provides fairly acceptable predictions while determining the pressure drop and concentration profile for various effluent concentrations and flow velocities. Furthermore, the optical observations made at the horizontal pipeline flow are used for validation of 3D simulation results for both air/water and water/sand horizontal flow systems where the slug and slurry flow conditions are established. The vibration characteristics of gas/ liquid/ solid particles flow patterns in pipelines are also investigated in this work. **Keywords**: CFD, FLUENT, Pipeline, Slug, Slurry, Vibrations.

2.1 Introduction

The flow in pipeline or annuli are of great importance and widely applied in different industries, such as chemical process and petroleum industries, pipe line engineering, power plants, biomedical engineering applications, micro-scale fluid dynamics studies, food processing industries, geothermal flows and extrusion of molten plastics [6].

Among all other types of flow, water-solid slurry flow and water-air slug flow have become increasingly popular due to its numerous applications in different industries and enormous focus of society on reduction in environmental pollution. This type of multiphase flow frequently occurs in horizontal pipelines and channels [6]. Liquid-Solid two phase slurry flow has been applied to transport raw materials, waste and sludge which are in solid form [7], beneficiation in extractive metallurgy and mining plants [8], coal processing plants [9], fluidized beds [10], food and chemical plants, petroleum industries and many more. Slurry transportation system helps to reduce traffic, air pollution, noise, accidents along with saving on energy consumption and lesser ecological disturbance. On the other hand, slug flow is caused by aerated slugs of liquid that flow down a pipeline at the same velocity as the gas. Many different operations in an oil field can be at the root of slugging, such as pigging, start-up, blow-down and general transient effects [11].

These problems can occur in the chemical and process industries or in thermo-hydraulic engineering for nuclear power plants [12], but our focus here is on oil and gas production. In these pipelines, multiphase slug flows can develop across a broad range of gas and liquid flow rates and pipe inclinations. Slug initiation, including slug initiation prediction, has been studied by several

researchers. In one study, slug initiation prediction is determined by analyzing the stability of a stratified flow in a pipeline [13].

At the same time, computational fluid dynamics (CFD), which is a programming and computation method, is also being applied to investigate the behavior of two-phase flows [14]. Another study looked into slug initiation and growth using a turbulence $k-\omega$ model [15]. Unfortunately, however, the modeling of two-phase flows for studying liquid and gas phases is not only time- and labor-intensive, but also intensely difficult due to the involvement of advanced physics and mathematics computations. Typical issues related to slugging are equipment damage, reduced production, facilities damage, and operational problems with equipment such as pipelines and separator vessels. Given the wide array of these and other potential problems, it is crucial to have a firm grasp not only of the slugging operation itself but also of the mechanisms underlying it. Phase distribution is a key component when designing engineering structures, mainly due to its impact on the values of parameters like thermal load and pressure drop. It is thus important to know both the system's distribution and flow regime. To that end, dual-phase flow maps can aid in the defining of flow patterns that may occur under different boundary conditions [16].

The main benefit of these mapping tools is that they do not require the user to carry out extensive and complex numerical calculations. Instead, slug movement can be determined by alterations in the liquid slugs and gas bubbles flowing at the top of the liquid films, which combine to form slug units. Slugs moving at a greater velocity than that of average liquid can initiate strong vibrations, causing damage to equipment in the direction and assemblage centers [17].

Slug frequency, which is defined as the number of slugs flowing past a certain point in a pipeline within a certain period of time, is an important factor in determining potential operational

difficulties such as pipe vibration and instability, fluctuations in wellhead pressure, and flooding of downstream facilities. Moreover, high slug frequency can cause pipe corrosion [18].

Our study will focus on pipeline vibration caused by unsteady flow, flow directional changes, pipe diameter, etc., in the petroleum, natural gas and chemical industries. Severe pipeline vibrations can impact the operation of pipelines and lead to unsafe and even hazardous conditions. Although pipe vibration is catching the attention of increased numbers of people in the industry, the majority of investigations into the phenomenon thus far have been on pipe vibration due to mechanical vibration sources. The cause of fluid vibration in pipelines has been studied with the help of various theoretical methods. For the sake of simplification and assumption, some results from some these approaches will be used here as references. Fluid vibration may present in several different forms, such as gas-liquid flow vibration, high-speed flow vibration, fluid pulsation, and flow vibration outside the pipeline [19].

Most existing studies focus on flow-induced vibrations (FIV) (impacts on internal flow from external current), whereas less attention has been allotted to internal flow, slug surge, and external current.The main aim of the current investigation into issues related to fluid structure interaction (FSI) is to develop a methodology that explains the basic physics of (FSI), along with the impact of the phenomenon on subsea piping parts. The accumulated data from this study (as well as studies in the future) will help to reformulate and revise the FSI model and its capabilities. Potential areas of improvement are to include Reynolds numbers and to show how free stream turbulent intensity levels impact subsea piping [20].

2.2 Mathematical models

The Eulerian multi-phase model of granular version is used in the current study. Although several different factors can be involved, the choice of a suitable model relies primarily on the range of volume fraction α_q of the solid phase under consideration. Hence, given the high value of volume fraction used here, the granular version emerges as the most appropriate. This approach helps to indicate the effects of friction and collusion among particles, an ability that is particularly desirable in high-concentration slurries with different sized grain [21].

2.2.1 Multi-phase Model

The Eulerian multi-phase model enables the modeling of different types of interactive phases, such as solids, liquids or gases, or any combination of these three states. Unlike the Eulerian-Lagrangian treatment, which is utilized in discrete phase models, the Eulerian approach is applied to individual phases [21].

2.2.1.1 Volume Fractions

Multi-phase flow, which can be described as "interpenetrating continua incorporate[ing] the concept of phasic volume fractions", is indicated here by α_q. [21]. Volume fractions indicate the area covered by each phase, while conservation laws pertaining to mass and momentum are satisfied by the phases. Furthermore, conservation equations can be calculated either by averaging

the local balance for each phase or by applying the mixture theory [22]. Phase q, V_q volume is stated as:

$$V_q = \int \alpha_q \, dv \tag{2-1}$$

where

$$\sum_q^n = 1 \alpha_q = 1 \tag{2-2}$$

Furthermore, phase q's effective density is calculated as:

$$\hat{\rho}_q = \alpha_q \rho_q \tag{2-3}$$

with ρ_q being phase q's physical density.

2.2.1.2 Conservation Equations

To designate general instances of n-phase flow, some equations for fluid-fluid and granular multi-phase flows are given below.

2.2.1.2.1 Continuity Equation

Here, the volume fraction for each phase is given in the following continuity equation:

$$\frac{1}{\rho rq}\left[\frac{\partial}{\partial t}\left(\alpha_q \rho_q\right) + \nabla.\left(\alpha_q \rho_q \ \underrightarrow{\vartheta_q}\right) = \ \sum_{q=1}^{n}(\dot{m}_{pq} - \dot{m}_{qp})\right] \tag{2-4}$$

where ρ_{rq} denotes the phase reference or volume averaged density of the q^{th}phase and

the solution domain, respectively, $\dot{m}_{pq}$ characterizes the mass transfer from the p^{th} to the q^{th} phase, and $\dot{m}_{qp}$ characterizes the mass transfer from the p^{th} to the q^{th} phase.

2.2.1.2.2 Fluid-Fluid Momentum Equations

Conservation of momentum for the fluid phase, q, is calculated as:

$$\frac{\partial}{\partial t}\left(a_q\rho_q\overrightarrow{\vartheta_q}\right)+\nabla.\left(a_q\rho_q\overrightarrow{\vartheta_q}\overrightarrow{\vartheta_q}\right)\ =-a_q\nabla_P+\nabla.\tau_q+a_q\rho_q\vec{g}+\sum_{q=1}^{n}\left\{k_{pq}\left(\overrightarrow{\vartheta_p}-\overrightarrow{\vartheta_q}\right)+\dot{m}_{pq}\overrightarrow{\vartheta_{qp}}-\dot{m}_{qp}\overrightarrow{\vartheta_{qp}}\right\}+\left(\overrightarrow{F_q}+\vec{F}_{lift,q}+\vec{F}_{vm,q}\right) \quad (2\text{-}5)$$

where $\vec{g}$ denotes gravity-driven acceleration, τ_q denotes the q^{th} phase stress-strain tensor, $\overrightarrow{F_q}$ denotes an external body force, $\vec{F}_{lift,q}$ indicates lift force, and $\vec{F}_{vm,q}$ is virtual mass force.

2.2.1.2.3 Fluid-Solid Momentum Equations

In 1960, Alder and Wainwright [23]. published a research study which presented a multi-fluid granular model. Their work is used in this present study to describe the flow behavior of a fluid-solid mixture. As can be seen, the conservation of momentum for the fluid phases is similar to Equation (2-5). The s^{th} solid phase is calculated as follows:

$$\frac{\partial}{\partial t}\left(a_s\rho_s\overrightarrow{\vartheta_s}\right)+\nabla.\left(a_s\rho_s\overrightarrow{\vartheta_s}\overrightarrow{\vartheta_s}\right)\ =-a_s\nabla_P-\nabla p_s+\nabla.\tau_s+a_s\rho_s\vec{g}+\sum_{q=1}^{n}\left\{k_{ls}\left(\overrightarrow{\vartheta_l}-\overrightarrow{\vartheta_s}\right)+\dot{m}_{ls}\overrightarrow{\vartheta_{ls}}-\dot{m}_{sl}\overrightarrow{\vartheta_{sl}}\right\}+\left(\overrightarrow{F_s}+\vec{F}_{lift,s}+\vec{F}_{vm,s}\right) \quad (2\text{-}6)$$

where p_s is the s^{th} solids pressure, k_{ls}= k_{sl} is the momentum exchange coefficient between fluid and solid phase l and solid phase s, and n denotes the number of phases.

2.2.2 Solids Pressure

When granular flows are in the compressible regime (such as when the solid's volume fraction is lower than the maximum allowed value), a solid's pressure can be measured individually and then substituted for ∇_{ps}, which is the pressure gradient term from the granular-phase momentum equation. Moreover, given that a Maxwellian velocity distribution is applied to the particles, the factor of granular temperature is thus included in the model:

$$p_s = a_s \rho_s \theta_s + 2\rho_s(1 + e_{ss}) a_s^2 g_{o,ss} \theta_s \tag{2-7}$$

where e_{ss} denotes the restitution coefficient of particle collisions, $g_{o,ss}$ is the radial distribution function, and θ_s the granular temperature. A default value of 0.9 for e_{ss} is applied; however, this can be changed according to particle type. Furthermore, the granular temperature, θ_s , is shown to be proportional to the fluctuating particle motion's kinetic energy, while the function $g_{o,ss}$ presents as a distribution function which determines the steady alteration from the compressible state of $a < a_{s,max}$, such that the area between the solid particles demotes to an incompressible state [23].

Here, $a = a_{s,max}$,, indicating that no additional decreases in area are possible. Although the default for $a_{s,max}$, is the value of 0.63, this can change during the process of setting up the problem [24].

2.2.3 Solids Shear Stress

Particle momentum exchange due to translation and collision can lead to solids stress tensor containing shear and bulk viscosities. Moreover, viscosity, as a frictional component, may contribute to the viscous-plastic transition which can occur if solid-phase particles achieve a maximum solid volume fraction. To give the solids shear viscosity (μ_s), we can add collisional and kinetic parts, as well as an optional frictional part, as shown in the following equation:

$$\mu_s = \mu_{s,col} + \mu_{s,kin} + \mu_{s,fr} \tag{2-8}$$

where $\mu_{s,col}$ indicates shear viscosity due to collision, $\mu_{S,kin}$ denotes kinetic viscosity, and $\mu_{s,fr}$ is frictional viscosity. The shear viscosity's collisional portion can thus be modeled as:

$$\mu_{s,col} = \frac{4}{5} a_{s\rho sds} g_{o,ss}(1 + e_{ss}) \left(\frac{\theta s}{\pi}\right)^{\frac{1}{2}} \tag{2-9}$$

with the kinetic viscosity default expression stated as:

$$\mu_{s,kin} = \frac{a_s d_s \rho_{s\sqrt{\theta_s \pi}}}{6(3-e_{ss})} \left[1 + \frac{2}{5}(1 + e_{ss})(3_{ess} - 1) a_s g_{o,ss}\right] \tag{2-10}$$

Here, frictional viscosity can be added through the expression:

$$\mu_{s,fr} = \frac{p_s \sin \emptyset}{2\sqrt{I_{2D}}} \tag{2-11}$$

2.3 The Reynolds Stress Model (RSM)

The Reynolds stress equation model (RSM) is the most complete of the classical turbulence models. Instead of applying the isotropic eddy-viscosity hypothesis, the RSM resolves the

Reynolds-averaged Navier Stokes equations by using transport equations for Reynolds stresses, along with a dissipation rate equation. Hence, four extra transport equations are needed for the 2D flows, while seven extra transport equations have to be solved in 3D.

However, because the RSM takes into consideration the impacts of streamline curvature, swirl, rotation, and rapid changes in strain rate using a more in-depth approach than either one- or two-equation models, it has a higher likelihood to arrive at more accurate predictions for complex flows. Nonetheless, the accuracy of this model's predictions can be affected by closure assumptions used to show different terms in the Reynolds stresses transport equations [24].

In this regard, pressure-strain and dissipation-rate term modeling is especially difficult, thus leading to the assumption that these measurements can significantly skew RSM prediction accuracy. Although the RSM might not consistently give results that are better than simpler models with regard to all flow classes, the approach is still useful when the targeted flow features result from anisotropy in the Reynolds stresses, such as cyclone flows, swirling flows in combustors, rotating flow passages, and stress-induced secondary flows in ducts [25].

2.3.1 Reynolds Stress Transport Equations

The exact form of the Reynolds stress transport equations may be derived by taking moments of the exact momentum equation.

$$\underbrace{\frac{\partial}{\partial t}\left(\rho\overline{u_l'u_l'}\right)}_{Local\ Time\ Derivative} + \underbrace{\frac{\partial}{\partial x_k}\left(\rho u_k\overline{u_l'u_l'}\right)}_{c_{ij}\equiv Convection} = -\underbrace{\frac{\partial}{\partial x_k}\left[\rho\overline{u_l'u_l'u_k'} + p\left(s_{kj}u_l' + s_{lk}u_l'\right)\right]}_{D_{T,ij}\equiv Turbulent\ Diffusion} +$$

$$\underbrace{\frac{\partial}{\partial x_k}\left[\mu\frac{\partial y}{\partial x_k}\left(\overline{u_l'u_l'}\right)\right]}_{D_{L,ij}\equiv Molecular\ Diffusion} - \rho\underbrace{\left(\overline{u_l'u_k'}\frac{\partial u_j}{\partial x_k} + \overline{u_l'u_k'}\frac{\partial u_j}{\partial x_k}\right)}_{P_{ij}\equiv Stress\ Production} -$$

$$\underbrace{\rho\beta\left(g_i\overline{u_j^{\prime}\theta}+g_i\overline{u_j^{\prime}\theta}\right)}_{G_{ij}\equiv Buoyancy\ Production}+\underbrace{\overline{p\left(\frac{\partial u_l^{\prime}}{\partial x_J}+\frac{\partial u_l^{\prime}}{\partial x_l}\right)}}_{\emptyset_{ij}\equiv Pressure\ Strain}-\underbrace{2\mu\overline{\frac{\partial u_l^{\prime}}{\partial x_k}+\frac{\partial u_l^{\prime}}{\partial x_k}}}_{\in_{ij}\equiv Dissipation}-$$

$$\underbrace{2\rho\Omega_k\left(\overline{u_j^{\prime}u_m^{\prime}}\in_{ikm}+\overline{u_l^{\prime}u_m^{\prime}}\in_{jkm}\right)}_{F_{ij}\equiv Production\ by\ System\ Rotation}+\underbrace{S_{user}}_{User-Defined\ Source\ Term} \tag{2-12}$$

Noteworthy here is that various terms in G_{ij} ,$D_{L,ij}$, F_{ij}, and Fij require no modeling, even though $G_{T,ij}$, $G_{ij,}\emptyset_{ij}$ and $\in_{ij}$ need to be modeled to close the equations.

Below, the modeling assumptions that are needed to close the equation set are described in detail.

2.3.2 Modeling Turbulent Diffusive Transport

$D_{T,ij}$ may be modeled after the generalized gradient-diffusion model

$$D_{T,ij}=C_s\frac{\partial}{\partial x_k}\left(\rho\frac{k\overline{u_k^{\prime}u_l^{\prime}}}{\in}\frac{\partial\overline{u_l^{\prime}u_j^{\prime}}}{\partial x_l}\right) \tag{2-13}$$

This equation might, however, lead to numerical instabilities. Hence, we simplified the equation in FLUENT by applying a scalar turbulent diffusivity:

$$D_{T,ij}=\frac{\partial}{\partial x_k}\left(\rho\frac{\mu_t}{\sigma_k}\frac{\partial\overline{u_l^{\prime}u_j^{\prime}}}{\partial x_k}\right) \tag{2-14}$$

2.3.3 Linear Pressure-Strain Model

In FLUENT, we model the pressure-strain term, $\emptyset_{ij}$. The typical way to model $\emptyset_{ij}$ is to apply the decomposition as follows:

$$\emptyset_{ij} = \emptyset_{ij,1} + \emptyset_{ij,2} + \emptyset_{ij,w} \quad (2\text{-}15)$$

where $\emptyset_{ij,1}$ denotes the slow pressure-strain term (also called the return-to-isotropy term), $\emptyset_{ij,2}$ refers to the rapid pressure-strain term, and $\emptyset_{ij,w}$ indicates the wall-reflection term.

As shown, the slow pressure-strain term, $\emptyset_{ij,1}$, can be shown as:

$$\emptyset_{ij1} \equiv -C_{1\rho}\frac{\epsilon}{k}\left[\overline{u_l' u_j'} - \frac{2}{3}\delta_{ij}K\right] \quad (2\text{-}16)$$

where C_1 = 1.8.

Meanwhile, the rapid pressure-strain term, $\emptyset_{ij,2}$, can be modeled as:

$$\emptyset_{ij,2\equiv} C_2\left[\left(P_{ij} + F_{ij} + G_{ij} + C_{ij}\right) - \frac{2}{3}\delta_{ij}(P+G+C)\right] \quad (2\text{-}17)$$

with C_2 = 0.60, $P_{ij,}F_{ij,}C_{ij\,,}$ and C_{ij} being defined as previously shown in Equation (2-12), namely P = $\frac{1}{2}P_{kk}$, $G = \frac{1}{2}G_{kk}$, and $C = \frac{1}{2}C_{kk}$. The wall-reflection term, $\emptyset_{ij,w}$, indicates the redistribution of typical stresses close to the wall. Specifically, it dampens the stresses perpendicular to the wall, but enhances the stresses parallel to it. The equations below model the term:

$$\emptyset_{ij,w} \equiv C_1'\frac{\in}{k}\left(\overline{u_k' u_m'}n_k n_m\delta_{ij} - \frac{3}{2}\overline{u_l' u_k'}n_j n_k - \frac{3}{2}\overline{u_l' u_k'}n_i n_k\right)\frac{k^{\frac{3}{2}}}{C_{l\in d}}$$

$$+C_2'\left(\emptyset_{km2}n_k n_m\delta_{ij}\frac{3}{2}\emptyset_{jk,2}n_j n_k - \frac{3}{2}\emptyset_{jk,2}n_j n_k\right)\frac{k^{\frac{3}{2}}}{C_{l\in d}} \quad (2\text{-}18)$$

where C_1'= 0.5, C_2' = 0.3, n_k is the x_k component of the unit normal to the wall, d is the normal distance to the wall, and $C_l = \frac{C_\mu^{\frac{3}{4}}}{k}$, where C_μ = 0.09 and k is the von $k^{árm\acute{a}n}$ constant (= 0.4187). Here, $\emptyset_{ij,w}$ is added to the Reynolds stress model by default.

2.4. Numerical method

2.4.1 Conservation Equations in Solid Mechanics

Solid mechanics is a field of physics that investigates how solids react when impacted by external loads.

2.4.2 Elasticity Equations

Fluid structure interactions typically lead to elastic or plastic deformations of solid structures, which is caused by flow-induced forces. Ideally, the material should have an elastic behavior that enables it to regain its original shape or arrangement following the application of the load. Although stress can vary linearly, according to strain amount, an elastic deformable solid must adhere to continuum mechanics. In other words, it must abide by the conservation law that states: the sum of the forces must equal to zero [26].

The forces cause a distribution of stress throughout the surface area. So, when a large force is applied, the material might surpass the limitations of the elastic region and thus could fail through fracturing or assuming plastic behavior. The type of stress to which a material is subjected can change according to the location where the force is applied. To resolve the issue of stress components, the most common approach is to apportion the elastic material into smaller elements [26]. The following calculations are intended for normal and shear stresses:

$$\frac{\partial_{\sigma x}}{\partial x} + \frac{\partial_{\tau xy}}{\partial y} + \frac{\partial_{\tau xz}}{\partial z} + x_b = 0 \qquad (2\text{-}19)$$

where ∂ denotes normal stress, τ indicates shear stress, and x_b represents body forces per unit of volume.

2.4.3 Fluid Structure Interaction

Fluid Structure Interaction (FSI) is a multi-physics area that studies the impacts of a flow's pressure fluctuations on a structure in terms of deformation and stress. It also investigates whether it is a solid.

2.4.4 Flow-induced Vibration

If pressure fluctuations against the pipe wall are sufficiently large, fluids being transported through subsea pipes can lead to a phenomenon known as flow-induced vibration (FIV). When dealing with FIV, the pipe's instability is heavily dependent on the pipe's end condition. The type of pipe most susceptible to FIV damage and failure is a straight pipe with fixed ends. If there is breaching of the critical velocity, FIV can cause the pipe to buckle, as shown in the following equation:

$$V_c = \frac{\pi}{L}\left(\frac{EI}{\rho A}\right)^{\frac{1}{2}} \tag{2-20}$$

where EI denotes constant flexural rigidity, ρ indicates fluid density, A represents the pipe's internal area, and L and is pipe length [26].

2.5. Methodology

2.5.1 Geometry and Mesh

In this study, numerical simulations were done using a horizontal pipe (3m in length and 0.05m in diameter). Given the importance of the mesh to the numerical solution, the material required specific and exacting characteristics in order to provide a solution that was both feasible and accurate. The Directed Mesh technique in ANSYS software was used to develop the material and demonstrated appropriateness for simulating a two phase flow in the horizontal pipe. More specifically, the Directed Mesh technique was chosen because of its ability to decrease both the computational time and the number of cells in comparison to alternative meshing techniques, as well as its ability to form grids parametrically in a multi-block structure. By employing the path mesh, the user can control and specify the number of divisions in the inlet cross-section, enabling the creation of quadrilateral faces. Furthermore, by applying a novel type of volume distribution, users can specify how many layers they want to have on the pipe. To generate volume mesh, hexahedral grid cells were created through the extrusion of quadrilateral faces along the length of the pipe at each layer, as shown in Figure 2-1. It was determined that a structured hexahedral grid was most appropriate in the present case, as such a grid enabled a fine cross-sectional mesh to be created without also requiring an equivalent longitudinal one. This approach was considered superior, as it offered a faster process convergence. Additionally, as the fluid domains were asymmetrical, a grid independency study was carried out based on the water's superficial velocity at the outlet. In a multiphase flow, superficial velocity is the ratio of the velocity and the volume fraction of the considered phase. Hence, actual velocity of phase = (Superficial velocity of phase)/ (volume fraction of phase).

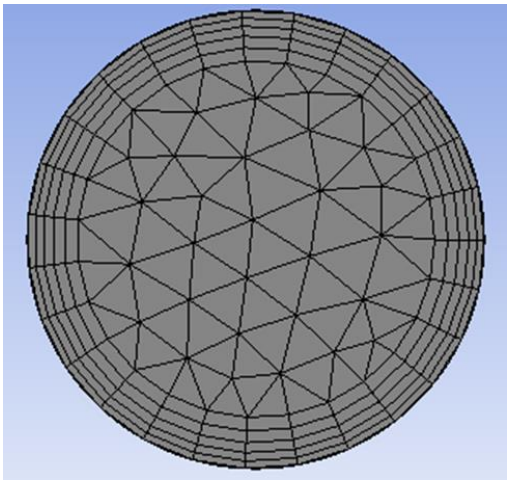

Figure 2-1 Computational mesh used for simulation

2.5.2 Boundary Conditions

At the gas and liquid inlets, uniform velocity inlets were used as boundary conditions. As well, an atmospheric pressure outlet condition was determined for the outlet to prevent any issues related to backflow at the tube's outlet, and a no-slip boundary condition was applied at the tube walls. The effect of the gravitational force on the flow was also taken into consideration. Overall, the initial volume fraction of gas was altered according to changes in the pipeline's gas velocity

2.5.3 Convergence Criteria

FLUENT is software for simulating flow utilizing pre-stated boundary conditions and a turbulence model. In order to terminate the A iteration, we use a convergence criterion of 10^{-6}. Furthermore, to guarantee the desired degree of accuracy as well as stability and convergence of the iterative process, we use second-order upwind discretization for the momentum equation, along with a first upwind discretization for volume fraction, turbulent kinetic energy and dissipation.

2.6. Results and Simulation

2.6.1 Pressure Drop

In designing a pipeline, pressure is a crucial parameter. Specifically, a system's pressure readings are essential measurements in calculating the pumping energy in a flow. In the present study, and as shown in Figuir 2-2, pressure was obtained from CFD along the pipe between the inlet and outlet. Similar to work performed by Kaushal, the diameter of the pipe used was 0.054, with a flow velocity of up to (5 m/s). We found that the pressure drop for single-phase flow rises as the flow velocity rises. The results indicate that there is very good agreement with the experimental data, showing < 9% error.

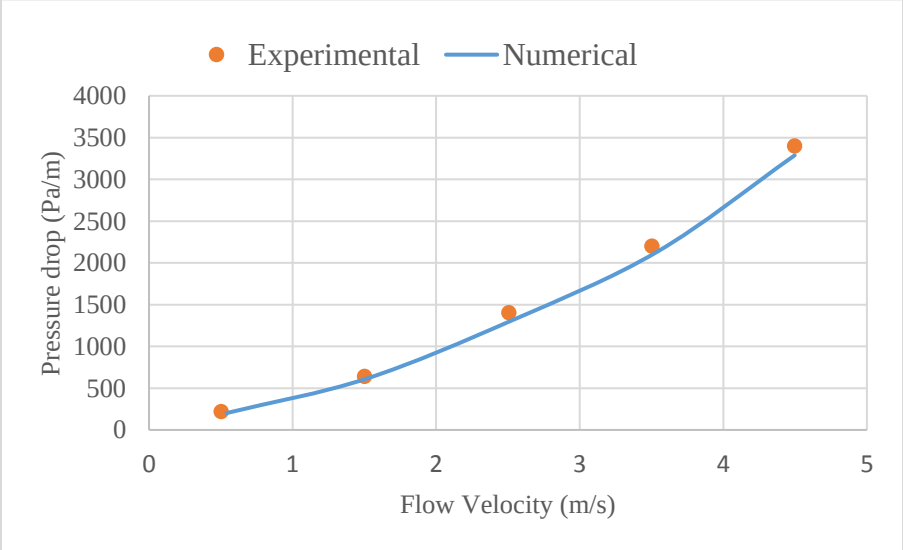

Figure 2-2 Pressure drop obtained from CFD compared to pressure drop measured from data with Flow velocity (m/s)

2.6.2 Pressure Gradient

Figure 2-3 depicts a CFD simulation of Eulerian multiphase model pressure gradients in a two phase slug flow. As can be seen in the figure, the x axis indicates gas superficial velocity, while the y axis indicates pressure gradient. Also shown (for comparative purposes) with experimental data from studies done by Kago et al. and Nadler and Mewes .Using a diameter of 0.05, two sets of simulations showed experimental results of gas velocities and constant liquid velocity. It is clear from figure 2-3 that the CFD outcomes demonstrate nearly the exact same trends as those stemming from the experimental data .The similarities in outcomes thus affirm the suitability of using CFD to pre-determine pressure gradients in gas and liquid slug flows.

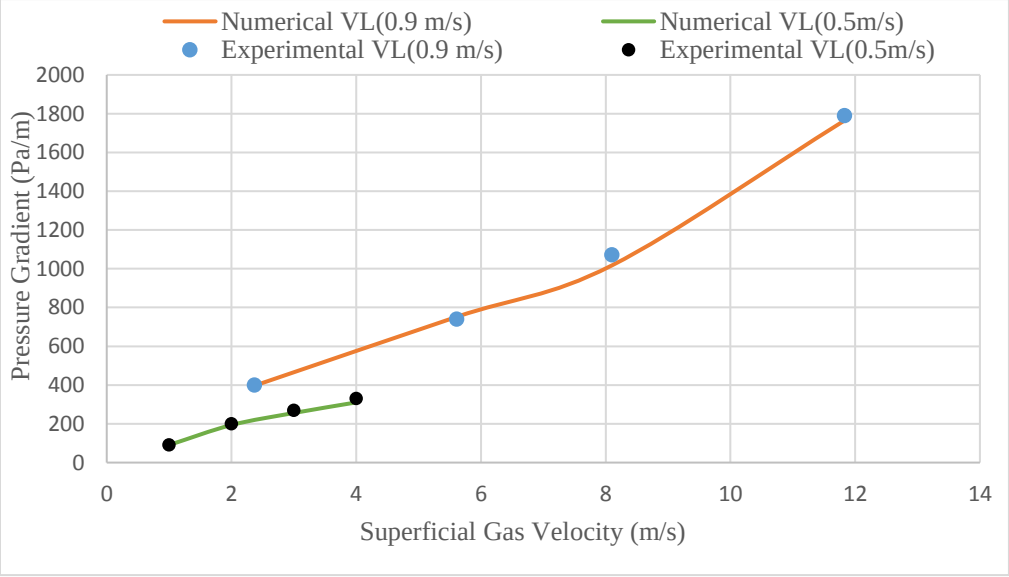

Figure 2-3 Comparison between CFD pressure gradient and experimental data Nadler and Mewes (1995a) for air–water flow, D=0.059m with superficial gas velocity (m/s)

2.6.3. Sensitivity Analysis

2.6.3.1 Solid Concentration Contours

Figure 2-4 depict contours in a non-dimensional solid concentration on a vertical plane outlet. As can be seen, the 4 grain sizes display different efflux concentrations (C_{vf}) with a 3.1m/s mixture velocity. The vertical plane's solid concentration at the outlet point is revealed as a non-dimensional zed when applying the corresponding inlet efflux concentration shown in figure 2-4. Furthermore, the contours clearly illustrate how areas featuring the highest solid concentrations are positioned close to the wall at the bottom half of the pipe's cross-section when pertaining to small grain (i.e., particle) objects. The positioning of these areas, however, experience a constant movement upward as the grain particle sizes increase. This movement is likely caused by the rise in lift-force in objects positioned close to the wall, as has been formulated for larger grain/particle sized in the simulation tests. Moreover, because anomalies in validation data also occurred close to the wall areas during testing of larger grain/particle sizes, this indicates a need to model the lift coefficient employed in simulation tests on the variously sized grains. Additionally, it was noted how the spread in the solid concentration area was enhanced by boosting the efflux concentration and mixture velocity; this increase, however, revealed a somewhat reduced intensity.

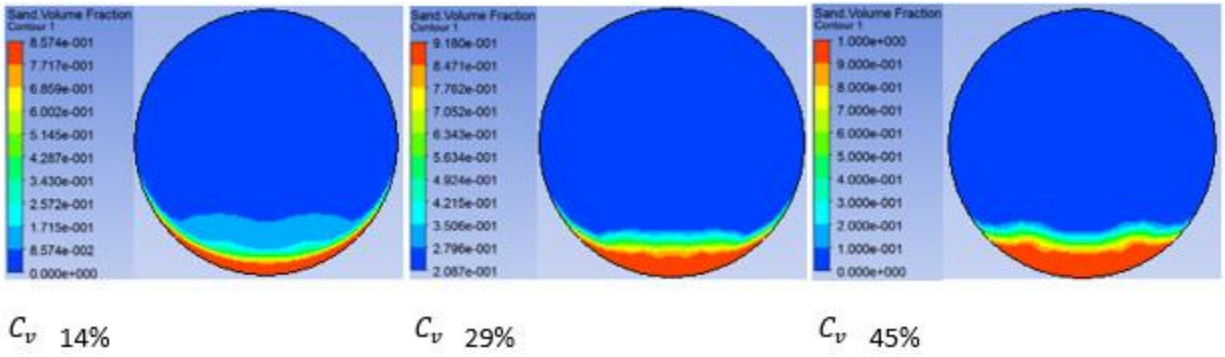

Figure 2-4 Sand concentration distribution at fully developed flow regime with 3.1 m/s mixture velocity. Cv = 14%, Cv = 29% and Cv 45%

2.6.3.2 Profiles of Local Solid Concentration

Experimental data from Gillies and Shook are compared with a local solid concentration profile of water-sand slurry flow from a simulation. The length of the pipe used in the experiment is 2.7 m and the diameter is 0.0532 m. The fluid (water) density is 9982 Kg/m^3, viscosity 0.001003 Kg/m, while the sand density is 3650 Kg/m^3. The wall material is aluminum and features a density of 2800 kg/m3 and a roughness of 0.2mm. Furthermore, the grain size or mean particle diameter is 0.18 mm, the mixture velocity is 3.1 m/s, and there are three distinct solid volumetric concentrations of 14%, 29% and 45%.

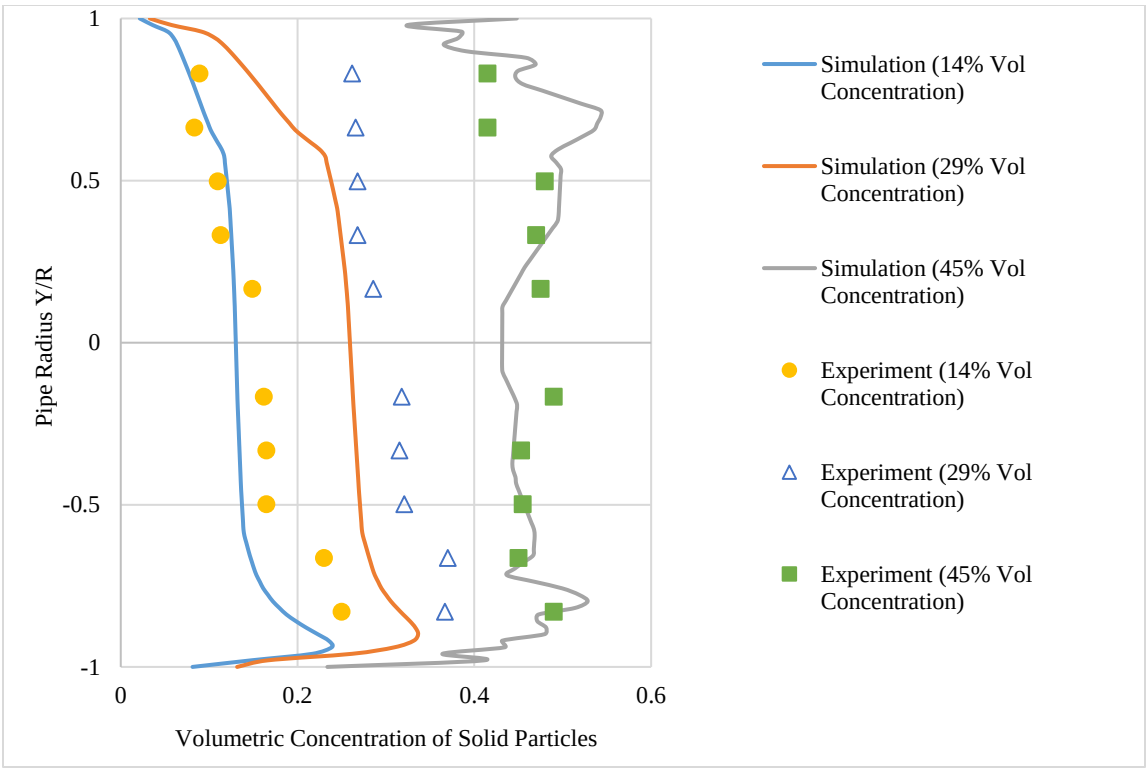

Figure 2-5 Comparison of simulated and measured values of local volumetric concentration of solid across vertical centerline for particle sizes 0.18 mm.

Figure 2-5 illustrates a comparison of particle sizes and volumetric concentrations of solid particles for the pipe radius Y/R. As shwon in the Figure 2-5, the simulated results show good agreement with the experimental values of grain sizes measuring 0.18 mm, but the simulated values differ somewhat from the experimental values when in close proximity to the wall, particularly in the bottom portion of the cross-section. A potential explanation for this occurrence is abrasive rounding of the large particles due to repeated passages. This could cause fines to be created and uniformly distributed within the pipe, leading to an increase in carrier density. However, because data related to this aspect of the experiment were not available in the reference research, the appropriate adjustments to reflect these data were not made during the simulations.

The deviations might also have resulted from the value of the static settled concentration (packing limit) applied in the simulations. Specifically, the 0.63 value used is most suited to calculations pertaining to very fine grain sizes. To minimize deviations with experimental results, analysis of newer boundary conditions at the wall for slurry pipeline flows should therefore consider larger grain sand sizes.

2.6.3.3 Slug Body Length

Figure 2-6 shows simulation test outcomes for 3 different gas velocities, 3.1m/s, 3.5m/s and 4.1m/s with length of the pipe used 4m and the diameter is 0.051m. As depicted in the figure 2-6, the slug length stretches along the length of pipe, and there is a proportional relationship for air superficial velocity and slug length. Specifically, the prediction outcomes for slug length indicate that rises in air superficial velocity resulted in the lengthening of slugs.

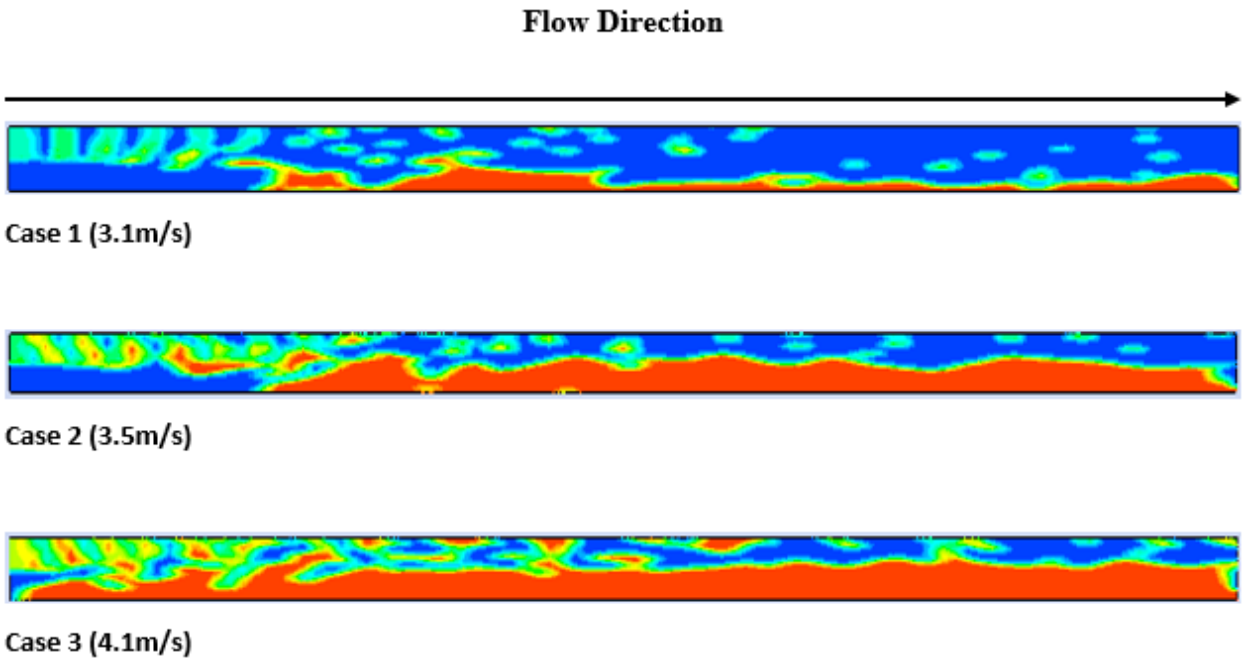

Figure 2-6 Slug length calculation of air-water slug flow

2.6.3.4 Pressure Drop

An important guideline for two phase pipeline design is pressure drop, especially with regard to losses and generated forces interacting with a pipe's inner surface. In the present work, pressure was first simulated and then stored in the pipe as a time series by applying ANSYS Software's field function. In the simulations, the superficial gas velocities were measured as 3.1, 3.5 and 4.1. As shown in Figure 2-7, a sudden pressure rebound occurred as a slug impacted the upper pipe wall, causing a pressure repulsion. This sudden increase in pressure pointed to the slug reaching the simulation's pressure sensor, whereas the abrupt pressure decrease pointed to the slug having passed the sensor. As illustrated in Figure 2-7, the simulation results show how decreases in pressure within the pipe became more pronounced as the superficial gas velocity increased, even as the water superficial velocity stayed the same.

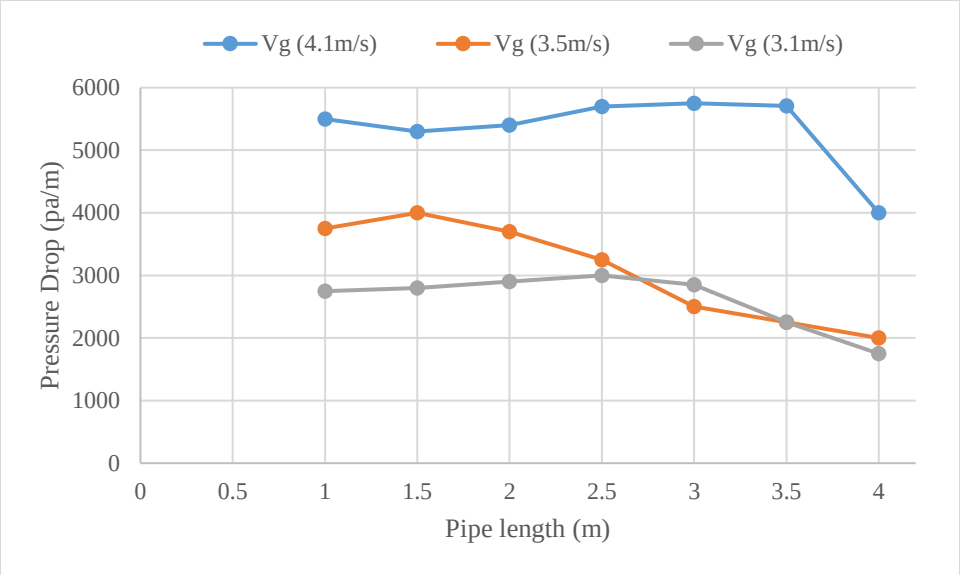

Figure 2-7 Pressure drop along the pipe for all Cases.

2.6.4. Fluid Structure Interaction (FSI)

2.6.4.1 Stress and Deformation

The fluid-structure interaction (FSI) of a static structural was modelled in ANSYS workbench by importing the fluid pressure data from Fluent to the static structure domain. The deformation was checked through a horizontal straight pipe of 3 m (in length) and 0.05 m (in diameter).The stress and total deformation of the pipeline due to the slug-flow induced vibration was analyzed and presented in a contour plot, which is presented in Figure 2-8. Growing waves in the gas-liquid stratified flow in horizontal pipe transformed to a roll waves, which is big enough to seal/bridge the pipe diameter resulting in air pockets and slugs. The effect of intermittent slug evolution and flow disturbances in rigid shape results in high pressure gradient. The pressure load to the structure

has been demonstrated to cause significant structural deformation in the FSI analysis as presented in Figure 2-8.

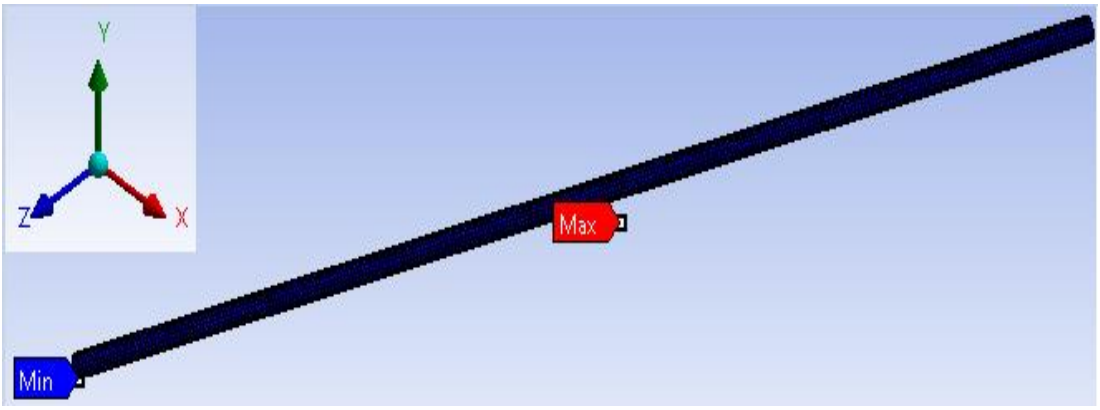

(A)

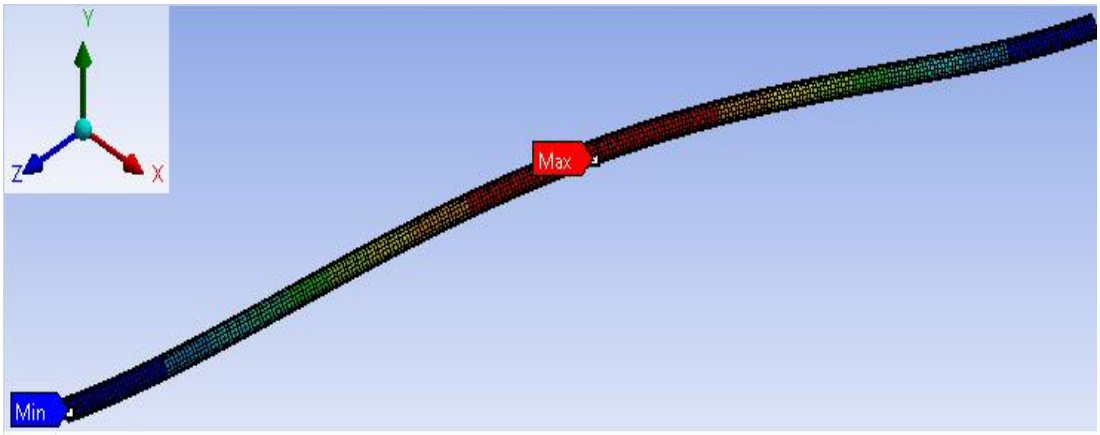

(B)

Figure 2-8 Deformation of straight pipeline: (A) Minimum deformation, (B) Maximum deformation

2.6.4.2 Profile of (FSI)

Figure 2-9 represents the total deformation with changing gas velocity. Deformation in pipeline increases with increasing gas velocity.

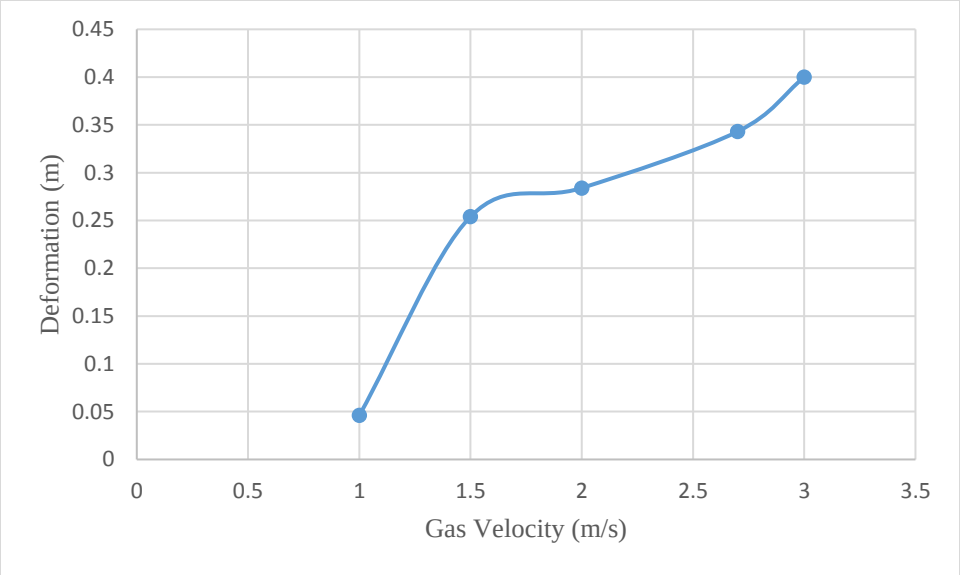

Figure 2-9 Total Deformation (m)

2.7 Conclusions

This work presented a numerical model aimed at achieving the qualitative study of a horizontal pipe's two-phase slug and slurry flows. FLUENT software (computational fluid dynamics (CFD) package) was used in the investigation. Given the large amount of computational operations that would have been required, three-dimensional simulation was simply too costly, so a model simulation was developed based on an Eulerian model and Reynolds stress model (RSM) turbulence. The results demonstrated all of the phenomena related to slug flow in a 3-D model. Overall, the comparison of pressure drops in pressure gradient measurements for both single-and two-phase flows in horizontal pipes indicate good agreement with the experimental data. Hence, this work adds to the knowledge base around two-phase slurry flows that feature various sized particles.

However, due to some data scatter related to flow parameters (particularly in slurry flows with larger particle sizes), the model applied here requires some revisions. High levels of vibration can be caused by instability arising from two-phase flows (i.e., slug flow), which can then shorten the pipe's fatigue life. Because of the complexity of slug flow behavior, engineers have had difficulty over the years trying to develop a methodology that can anticipate the impact of slugs. Furthermore, the present work demonstrated that the approach has application in problems related to fluid structure interaction in the oil and gas industry. Flow-induced vibration (FIV) is a common occurrence in this industry as a result of the strong coupling of structure and flow. Slug flow can generate large amplitude deformation such that the structure of the flow is altered and can create a catastrophic event However, assessing hydraulic characteristics and quantitatively investigating pipeline slug flow can benefit from more accurate simulations.

Chapter 3

Analyses of Slug flow Through Annular Pipe

Hassn Hadia[1], Rasel Sultan[1], Mohamed Rahman[2], John Shirokoff[1]

[1]Faculty of Engineering and Applied Science, Memorial University of Newfoundland, Canada

[2] Faculty of Petroleum Engineering, Texas A&M University at Qatar, Doha, Qatar

Abstract

Slug flow pattern through straight annular pipe (2- 4.5 m long, 0.02- 0.088 m inner, and 0.04-0.12 m outer diameter) and straight horizontal pipe (2-15 m long and 0.05 m internal diameter), is discussed in this study. The paper presents and investigates numerical results from computational fluid dynamic (CFD) simulations of the air-water slug flow where concentric annular pipe geometry with horizontal orientation is used. The Eulerian model and volume of fluid (VOF) model with the Shear-Stress-Transport (SST) model option of turbulence closure are used to simulate slug flow. A commercial CFD package ANSYS 16.2 is used to model slug flow. Additional investigations include comparing CFD predictions along with experimental measurements in the literature, and performing sensitivity studies based on different parameters by changing liquid velocity, gas concentration and timing. Output parameters (such as pressure gradient; superficial velocity of liquid and gas, air volumetric fraction) are analyzed during the process. Overall good agreement found in this simulation with experimental data for slug flow in annular pipe.

Keywords: CFD, FLUENT, VOF, Annular Pipe, Slug flow

3.1 Introduction

For companies working in the Oil and Gas (O&G) field, annular pipe slug flow can be a crucial factor in applications related to drilling equipment [27]. In fact, annular pipe flow can offer an overview of issues in relation to advanced stages of turbulent slug flow. Concentric annular pipe flow features dual boundary layers that function to distribute a range of turbulence qualities, with pipe and channel flows serving as the limiting versions of annular pipe slug flow [28].

Overall, the O&G industry experiences a broad spectrum of issues around the transportation of fluids (including multiphase flow) either through pipelines or annular pipes. That being said, multiphase flow domains can now utilize advanced technology in the form of fluid dynamic software packages that enable engineers to tailor pipe designs to exact specifications in order to predict the output of O&G systems [29]. Such specifications are useful, given that unstable pipeline flow can cause operational issues that ultimately increase expenditures. So, for instance, liquid flows that contain large slugs are considered unstable and generally require a separator to deal with them; otherwise, they could further evolve into hydrodynamic slugs or even a mass of slugs [30].

The mechanisms undergirding slug growth are currently not well understood. Typically, slugs are the end result of disturbances in liquid and gas plugs. Slug flow occurs in liquid-gas two-phase flows in a horizontal pipeline and annular pipe across a range of intermediate flow rates. The slug/plug distribution depends on a variety of factors, such as fluctuations in gas/liquid velocity, pigging, and even the terrain [30]. Each slug/plug unit is made up of a gas bubble and aerated

liquid slug. Bubble size depends mainly on positioning, with smaller bubbles occurring immediately in front of slugs, and larger ones trailing behind [31].

However, unlike the bubbles, slug lengths are consistent even through pressure drops in the pipeline. Because gas and liquid multiphase flow has become so common in, for instance, O&G transport as well as other critical industries involving geothermal heating, there has been an increase in the published literature dedicated to the topic of flows in pipes and tubing with diameters smaller than 10 cm. However, data pertaining to large diameter pipelines is nearly non-existent in the literature [32]. Further adding to the problem of data gap is the inconsistency of slugs in two-phase gas/liquid, which necessitates very complicated simulations involving, among other measurements, the flow field geometry of flow regimes or flow patterns [33]. Additional issues can arise when attempting to assess the phase tile distribution, as well as factors like pressure drop, pressure gradient, and heat/mass transfer [34].

Direct numerical simulations (DNS) solve the main equations without the use of models, but they can be very time-consuming. This is because all flows can be described as 'turbulent', and turbulent flows contain immensely different magnitudes of time scales. Consequently, calculation times become unviable due to the fineness of the mesh resolution. In these instances, modeling can be used to consider any turbulent effects. In fact, turbulence modeling has recently become the primary focus of single-phase CFD research [35].

While in Ghosh et al. looked at the need for Multiphysics flow field information for economic design and optimization of operating conditions in so doing, they applied CFD to simulate the air-water flow situation [36]. Kaushik et al. [37] utilized the CFD software package FLUENT 16.2 to simulate the annular flow through horizontal pipes and succeeding in matching the simulated data and experimental results. They also carried out a simulation to investigate annular flow under

conditions of sudden expansion and contraction. In analyzing the profiles of volume fraction, velocity, pressure, and the fouling characteristic, the researchers presented a CFD analysis of core annular flow through pipeline and talked about the distribution of pressure, velocity and volume fraction, along with the fouling characteristic. Feasible operation conditions were then suggested, but these works are simulated by the Shear-Stress-Transport (SST) model and did not mention the effect of annulus thickness on the annular flow [38]. Ghosh used the Eulerian model to simulate core annular flow through a pipe and discussed additional flow specifications and the impact of annulus thickness on core annular flow. As in their results likewise pointed to feasible operational conditions for pipe design [38].

In this present study, the Eulerian model and Volume of Fluid (VOF) method with the Shear-Stress-Transport (SST) turbulence model have been implemented, employing the commercial ANSYS 16.2 software to simulate the horizontal sections of annulus pipe and pipeline for air-water slug flow. The objective has been to investigate to validate our model with different experimental data, also to evaluate volume fraction profile with time, in two different cross sections along the length of the pipes.

3.2. Mathematical modeling

In this work, we apply formulations that indicate the range of fluid-flow. Equations (3-1) and (3-2) (Navier-Stokes equations) refer to various flow types and can be solved for nearly all flows for CFD models [39]. We also use (e.g., energy and turbulence equations) to simulate slug:

$$\frac{\partial \rho}{\partial t}+\nabla \cdot (\rho u) = 0 \qquad (3\text{-}1)$$

$$\frac{\partial \rho u}{\partial t} + \nabla \cdot (\rho u u) = -\nabla P + \nabla + \nabla \cdot \tau + \rho g \quad (3\text{-}2)$$

where ρ denotes density, u denotes instantaneous velocity, p indicates pressure, τ refers to viscous stress tensor, and g describes the gravity vector.

3.2.1 The governing equations

Any flow quantity f is split into mean and fluctuating component as $f = \bar{f} + f''$ with $\bar{f''} = 0$ and $\check{f} = \frac{\overline{\rho f}}{\bar{\rho}}$ .The ($\bar{f}$) overbar quantity represents Reynolds averaged mean quantity [40].

3.2.1.1 Continuity Equations

Between phases, interface tracking can be achieved using a continuity equation to calculate the volume fraction of the phases. In calculating the q_{th} phase, the equation can take the form:

$$\frac{1}{\rho rq}\left[\frac{\partial}{\partial t}\left(\alpha_q \rho_q\right) + \nabla.\left(\alpha_q \rho_q \ \overrightarrow{\vartheta_q}\right) = \ \sum_{q=1}^{n}(\dot{m}_{pq} - \dot{m}_{qp})\right] \quad (3\text{-}3)$$

where ρ_{rq} is denotes the phase reference or volume averaged density of the q^{th}phase and the solution domain, respectively, $\dot{m}_{pq}$ characterizes the mass transfer from the p^{th} to the q^{th} phase, and $\dot{m}_{qp}$ characterizes the mass transfer from the p^{th} to the q^{th} phase [40].

3.2.1.2 Momentum Equation

As the momentum equation is solved for the entire domain. Moreover, the velocity field is seen to be identical across all cell phases, despite showing variations between the cells:

$$\partial \frac{\partial}{\partial t}(\rho\vec{v}) + \nabla \cdot (\rho\vec{v}\vec{v}) = -\nabla p + \nabla \cdot [\mu (\nabla\vec{v} + \nabla\vec{v}T)] + \rho\vec{g} + \vec{F} \quad (3\text{-}4)$$

In this equation, ρ is the density, v is the velocity, μ is the viscosity, p is the pressure, $\vec{g}$ is the gravitational acceleration, and $\vec{F}$ is the source term. Furthermore, any sizeable velocity difference between the phases may cause a reduction in the accuracy of the velocity computations closer to the interface [41].

3.2.2 The Volume Fraction Equation

The tracking of the interface(s) between the phases is accomplished by the solution of a continuity equation for the volume fraction of one (or more) of the phases. For the q^{th}phase, this Equation has the following form:

$$\frac{\partial \alpha q}{\partial t} + \vec{v}.\nabla_{\alpha q} = \frac{S_{\alpha q}}{\rho_q} \quad (3\text{-}5)$$

Where S is the interface between the two phases and ρ_q is the physical density of one phase (q). By default, the source term on the right-hand side of equation (3-5) is zero, but you can specify a constant or user-defined mass source for each phase [42]. The volume fraction equation was not solved for the primary phase; the primary-phase volume fraction will be computed based on the following constraint:

$$\sum_{q=1}^{n} \alpha q = 1 \quad (3\text{-}6)$$

3.2.4. The Shear-Stress Transport (SST) $k-\omega$ Model

This section presents the standard and shear-stress transport (SST) $k-\omega$ models. FLUENT also provides a variation called shear-stress transport (SST) $k-\omega$ model, so named because the

definition of the turbulent viscosity is modified to account for the transport of the principal turbulent shear stress. It is this feature that gives SST $k-\omega$ model an advantage in terms of performance over both the standard $k-\omega$ model and the standard $k-\omega$ model. Other modifications include the addition of a cross-diffusion term in the ω equation and a blending function to ensure that the model equations behave appropriately in both the near-wall and far-field zones [43].

3.2.4.1 Transport Equations for the SST $k-\omega$ Model

The SST $k-\omega$ model has a similar form to the standard $k-\omega$ model

$$\frac{\partial}{\partial t}(\rho k)+\frac{\partial}{\partial xi}(\rho k u_i)=\frac{\partial}{\partial xi}\left(T_k\frac{\partial k}{\partial xi}\right)+G_k-Y_k+S_k \tag{3-7}$$

and

$$\frac{\partial}{\partial t}(\rho w)+\frac{\partial}{\partial xi}(\rho w u_i)=\frac{\partial}{\partial xi}\left(T_w\frac{\partial w}{\partial xi}\right)+G_w-Y_w+S_w \tag{3-8}$$

In these equations, G_k represents the generation of turbulence kinetic energy due to mean velocity gradients, calculated G_w represents the generation of ω, calculated T_k and T_w represent the effective diffusivity of k and ω, respectively, which are calculated as described below. Y_k and Y_w represent the dissipation of k and ω due to turbulence, calculated D_w represents the cross-diffusion term, as described below. S_w and S_w are user-defined source terms [44].

3.2.4.2 Modeling the Effective Diffusivity

The SST $k-\omega$ model, effective diffusivities are:

$$T_k=\mu+\frac{\mu_t}{\sigma_k} \tag{3-9}$$

$$T_w = \mu + \frac{\mu_t}{\sigma_w} \tag{3-10}$$

where σ_k and σ_w represent turbulent Prandtl numbers for k and ω, respectively. Turbulent viscosity, μ_t, can be expressed as:

$$\mu_t = \frac{\rho_k}{w} \frac{1}{max\left[\frac{1}{\alpha^*}, \frac{\Omega F_2}{\alpha_1 w}\right]} \tag{3-11}$$

where

$$\Omega \equiv \sqrt{2\Omega_{ij}\Omega_{ij}} \tag{3-12}$$

$$\sigma_k = \frac{1}{F_1/\sigma k_{,1} + (1-F_1)/\sigma k_{,2}} \tag{3-13}$$

$$\sigma_k = \frac{1}{F_1/\sigma w_{,1} + (1-F_1)/\sigma w_{,2}} \tag{3-14}$$

Ω_{ij} denotes the average rate-of-rotation tensor while α^* indicates the coefficient damps. The turbulent viscosity for the blending functions, $F_1$and F_1, can be expressed as:

$$F_1 tanh(\Phi_1^4) \tag{3-15}$$

$$\Phi_1 = min\left[max\left(\frac{\sqrt{k}}{0.09_{wy}}, \frac{500_\mu}{\rho y^2 w}\right), \frac{4\rho k}{\sigma_{w,2} D_w^+ y^2}\right] \tag{3-16}$$

$$D_w^+ = max\left[2_\rho \frac{1}{\sigma_{w,2}} \frac{1}{w} \frac{\partial k}{\partial xj} \frac{\partial w}{\partial xj}, 10^{-2}\right] \tag{3-17}$$

$$F_2 = tanh(\Phi_2^2) \tag{3-18}$$

$$\Phi_1 = max\left[2\frac{\sqrt{k}}{0.09_{wy}}, \frac{500}{\rho y^2 w}\right] \tag{3-19}$$

where y indicates the distance to subsequent surfaces and D_w^+ denotes the positive component in the cross-diffusion term [44].

3.2.2.4.3 Modeling Turbulence Production

Production of k

G_k Indicates turbulence kinetic energy production and can thus be formulated similar to the standard $k-\omega$ model.

Production of ω

G_w indicates ω production and can be expressed as follows:

$$G_w = \frac{\alpha}{vt} G_k \tag{3-20}$$

As can be seen, this expression diverges from the standard $k-\omega$ model. The two models calculate α_∞ differently. Whereas in the standard $k-\omega$ model, α_∞ denotes a constant (0.52), in the SST $k-\omega$ model, α_∞ appears as:

$$\alpha_\infty = F_{1\alpha\infty,1} + (1 - F_1)\alpha_\infty, 2 \tag{3-21}$$

where

$$\alpha_\infty, 1 = \frac{\beta_{i,1}}{\beta^*_\infty} - \frac{k^2}{\sigma_{w,1}\sqrt{\beta^*_\infty}} \tag{3-22}$$

$$\alpha_\infty, 2 = \frac{\beta_{i,2}}{\beta^*_\infty} - \frac{k^2}{\sigma_{w,2}\sqrt{\beta^*_\infty}} \tag{3-23}$$

where ω denotes 0.41. Equations (3-27) and (3-28) show $\beta_{i,1}$ and $\beta_{i,2}$, respectively, as follows [44]:

3.2.5. Modeling the Turbulence Dissipation

3.2.5.1 Dissipation of k

Y_k indicates turbulence kinetic energy dissipation and can be expressed nearly the same way as the standard $k-\omega$ model [44]. The sole difference can be found in how we calculate for $f\beta^*$. Thus,

for the standard $k-\omega$ model, $f\beta^*$ can be calculated like a piecewise function, whereas for the SST $k-\omega$ model, $f\beta^*$ represents a constant that is equivalent to 1. Based on this,

$$Y_k = \rho\beta^* k_w \quad (3\text{-}24)$$

3.2.5.2 Dissipation of ω

Y_w indicates the dissipation of ω . It can be formulated like the standard $k-\omega$ model, except for how β_i and f_β are calculated. Whereas, for the standard $k-\omega$ model, β_i appears as a constant (0.072), in the SST $k-\omega$ model, f_β denotes a constant that is equivalent to (1) [45]. Therefore,

$$Y_k = \rho\beta w^2 \quad (3\text{-}25)$$

Instead of a constant, β_i can be expressed as:

$$\beta_i = F_1\beta_{i,1} + (1-F_1)\beta_{i,2} \quad (3\text{-}26)$$

where

$$\beta_{i,1} = 0.075 \quad (3\text{-}27)$$

$$\beta_{i,2} = 0.082 \quad (3\text{-}28)$$

while F_1 can be formulated using Equation (3-15).

3.3. Methodology

3.3.1 Geometry and mesh

Because the mesh can have a strong effect on the solver convergence and solution for each CFD simulation, the quality of mesh used should always be relatively high to enable convergence as

well as correct proportions for the simulation. In this study, the initial example showed that were created (i.e., 400,063 elements at the annular pipe but 397,485 at the cross-section of the pipeline). Additionally, regarding the time resolution, 0.001 was used as a time-step. This approach resolves the time resolution for measuring instruments employed by (A) and (B). In those instances, mesh featuring a 400,063 cell annular pipe geometry measuring 2 m in length and with a 0.02 inner, 0.04 outer m diameter (with measurements of the pipeline being 397,485 cell pipeline geometry, 5 m length/0.05 m diameter) is considered suitable in the inlet flow comprised of liquid and gas superficial velocities of 0.55 m/s and 1.65 m/s, respectively. However, in this work, we applied lower velocities. In the two cases, mesh refinement was performed according to the details below to verify the outcome from the mesh structuring.

Specifically, these simulations have been performed in a four-processor machine, with a simulation run-time of several hundred hours. This permits movement of the gas phase upwards (i.e. from the pipe bottom to the pipe top). The run-time can be decreased by adding processors that run in parallel. It is also worth noting that the strength of computers will likely increase exponentially soon. Our mesh was the type known as butterfly grid, as shown in Figure 3-1. For butterfly grip mesh, another mesh (Cartesian mesh) can be added to the central part of a pipe and used together with a cylindrical pipe. This approach necessitates the use of several blocks; however, it represents optimal grid quality in relation to mesh density and orthogonality. Although building this mesh can be more time-consuming, this can be mitigated by employing ANSYS software.

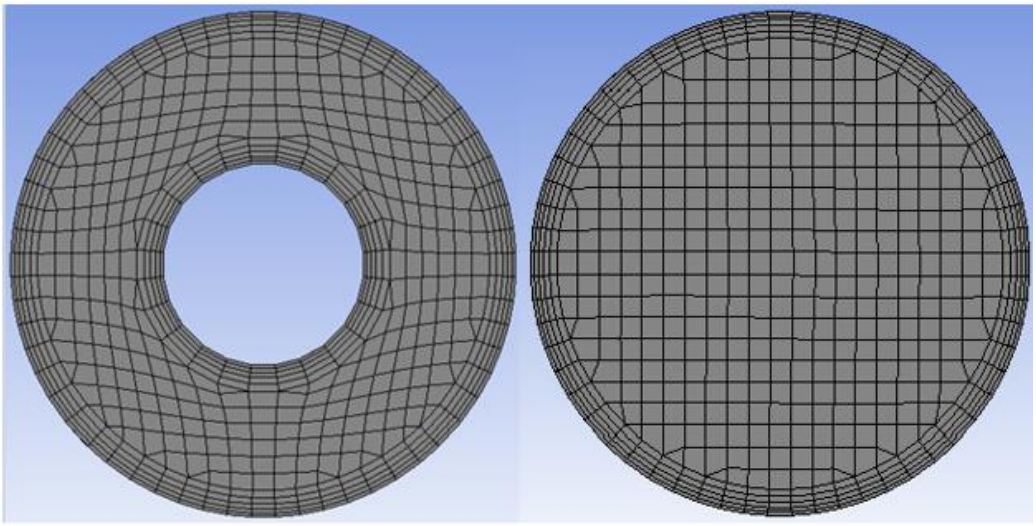

(A) (B)

Figure 3-1 Meshing of model used in CFD simulation (A) Mesh of Annular Pipe (B) Mesh of Pipeline

3.3.2 Mesh Independent

Mesh domain simplification is required, as we will only be able to resolve a mathematical model if we assume linearity. In other words, we must make sure the variables targeted for resolution are linearized for every cell. Such a requirement indicates that mesh made from finer material (which can be created through specific refinement stages) should be used in parts of the domain featuring physical properties that are assumed to be highly volatile. However, before developing a mesh structure with a relatively small number of elements and then performing analysis, we first make sure that the quality of the mesh as well as the model coverage can be realistically examined. The aim here is to recreate mesh structures that have a higher number of elements and then to repeat the analysis and perform a comparison of the results according to properties found in previous cases. So, for example, when a case features examining an internal flow through one or more

channels, we could potentially use pressure drops in critical regions for comparison purposes. Next, we would continue moving up to several elements that show results in good agreement with prior results. In this way, any issues that have emerged due to the mesh structure are removed and the best possible value related to element number can be arrived at to make the calculations faster. Figure 3-2 shows pressure changes in region Y caused by raising the number of elements. As can be seen, we would need approximately between 300,000 up to 700,000 elements to perform a study with valid outcomes.

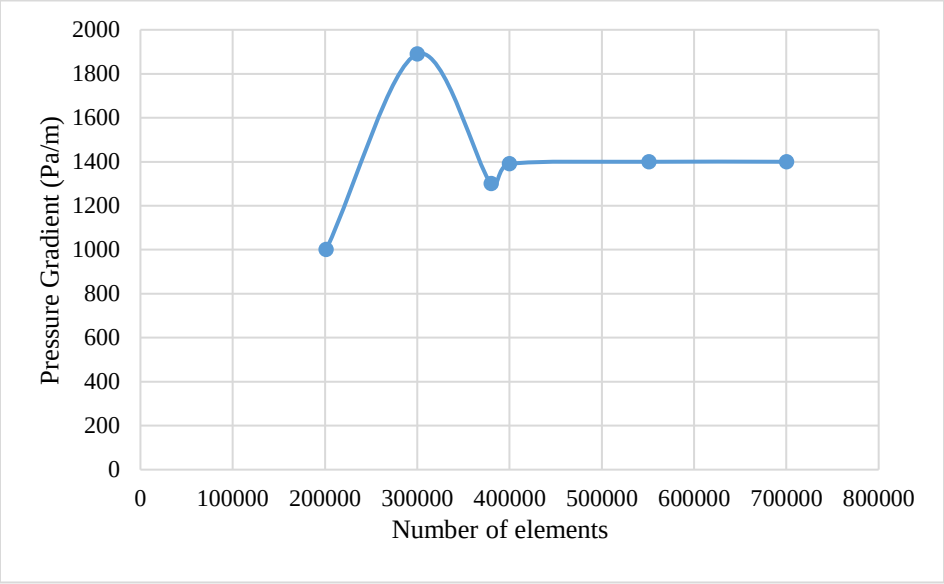

Figure 3-2 Mesh independence analysis

3.3.3 Boundary conditions

We used uniform velocity inlets to serve as boundary conditions for gas and liquid inlets. To prevent backflow near the tube's outlet, we implemented an atmospheric pressure outlet that included a no-slip boundary condition near the tube walls. As well, we also took into consideration

the flow's response to gravitational force flow, and demarcated the initial air volume fraction for all instances.

3.3.4 Convergence Criteria

FLUENT is software for simulating flow utilizing pre-stated boundary conditions and a turbulence model. To terminate the iteration, we use a convergence criterion of Error Digit expected. Furthermore, to guarantee the desired degree of accuracy as well as stability and convergence of the iterative process, we use second-order upwind discretization for the momentum equation, along with a first upwind discretization for volume fraction, turbulent kinetic energy and dissipation.

3.4. Results and Discussion

3.4.1 Velocity Profile in Annular Pipe

To look deeper into the curvature impact, we need to compare average axial velocity profiles in the entire cross-section of annuli for a variety of inner and outer radius ratios. As it can be seen comparison in Figure 3-3 with Nouri and Whitelaw (1994), the velocity profiles appear to be asymmetrical with a decided tilt in the direct of the inner wall. This so-called skewness is the result of maximum axial velocities in locales near the inner wall. Such locales edge closer towards the inner wall when the radius ratio drops from 0.04 to 0.02. In other words, the maximum velocity can be found at y= 0.271 m/s distance from the inner wall. Here, y/ξ indicates distance between inner and outer wall of the annular pipe.

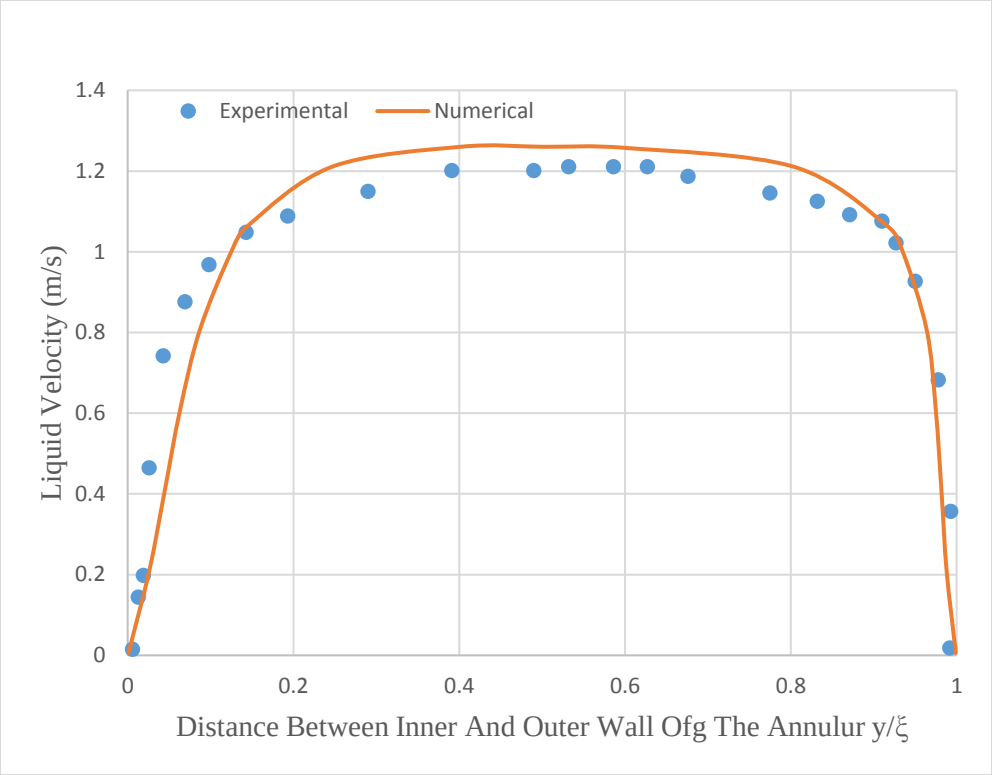

Figure 3-3 Comparison of liquid velocity between simulation and experimental data of Nouri and Whitelaw, 1994. For liquid Velocity 1.3 (m/s), Pressure outlet = 0 (Annular pipe)

3.4.2 Velocity Profile in Pipeline

Figure 3-4 illustrates Lewis' (2002) data, representing low/ high values for V_g = 0.55 m/s, with a fixed value of V_l =1.65 m/s and a pipe geometry of 0.05m diameter and 15.4m length. As can be seen, R/r indicates a normalized radial setting for pipe, r. This is calculated near to the vertical axis, stretching from the center of the pipe towards the probe, where R represents pipe radius. In this case, – 1.0 and 1.0 indicate the pipe's bottom and top, respectively. As can further be seen in Figure 3-4, the average liquid velocity indicates asymmetrical liquid velocity profiles. Here, the most pronounced velocities can be found near the top of the pipe. Again, the profile illustrated in Figure 3-4 demonstrates an identical character as the fully-developed turbulent flow profile and

includes a transition zone between them. Our simulation indicate that the mean superficial velocities correspond well to maximum liquid velocity.

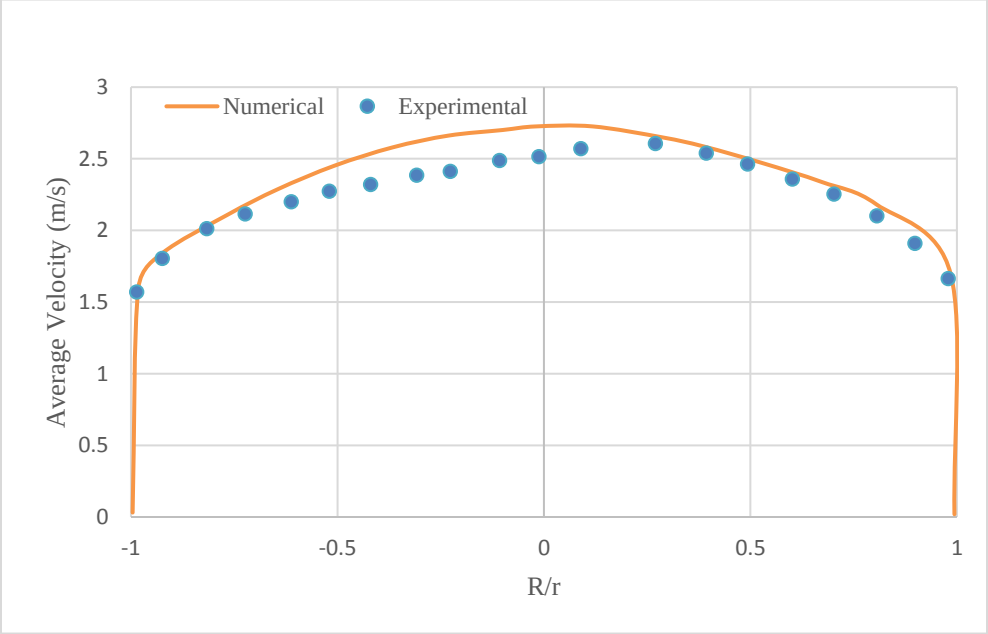

Figure 3-4 Comparison of mean liquid velocity at cross section simulation and experimental data of Lewis 2002. For gas velocity 0.55 m/s, liquid velocity 1.65 m/s Pressure outlet = 0 (pipeline)

3.4.3 Pressure Gradient

One of the key inputs in the design of slurry and slug flow pipelines is pressure gradient (in Pa/m). Figure 3-5 shows pressure gradients for two-phase slug flow predicted by CFD simulation. As can be seen, the x axis indicates the liquid superficial velocity, while the y axis indicates the pressure gradient. Experimental data from studies done by Wang (2015) is used for comparison purposes. Using a diameter of 0.059 and length 5 m in pipe, and experimental data from Ozbayoglu, M. E.& Omurlu, C. (2007) Using inner diameter 0.088, outer diameter 0.12 and length 4.57 m in concentric annuli, the liquid phase is considered as water (density 9982 Kg/m^3 and Air (density 1.225 kg/m^3). One set of simulation showed experimental results of liquid velocities ranged from (0.05- 1.16)

and constant gas velocity. The simulation results are compared with experimental data as . This figure shows how the pressure gradients predicted by CFD simulations and obtained from the experiment are well aligned. This proves the ability of CFD to predict pressure gradients for slug flows of gas and liquid. Moreover, because the pressure gradient level rose sharply as the liquid velocity increased, the impact of liquid velocity on pressure gradient can be assumed to be reasonably high.

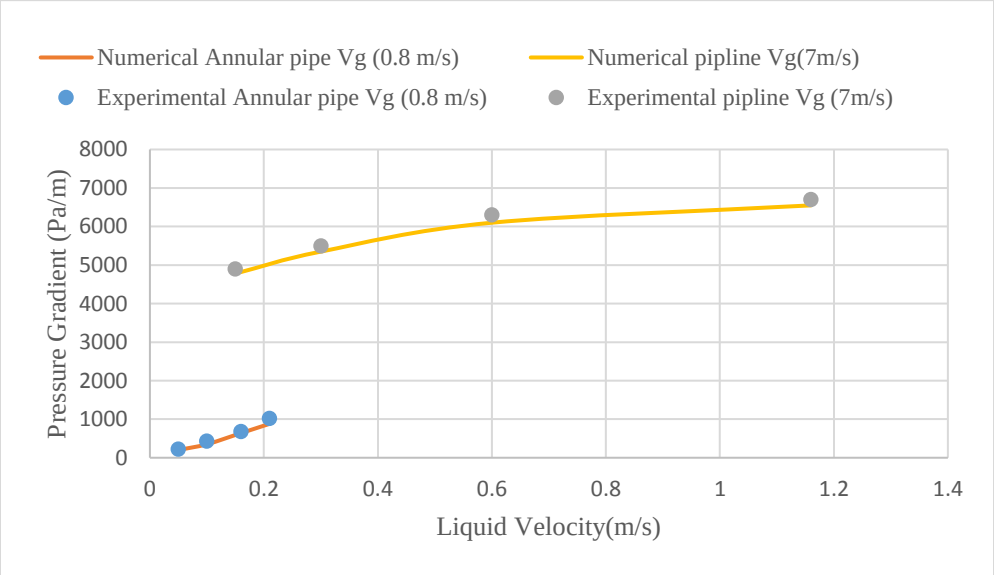

Figure 3-5 Pressure gradient obtained from CFD compared to pressure gradients measured from Experimental data in pipeline and concentric annuli

3.4.4 Profile Slug Volume Fraction in Annular Pipe

Figure 3-6 illustrates slug flow at 0.425 m/s air superficial velocity as well as 0.342 m/s water superficial velocity through horizontal annular pipe. As shown in Figure 3-6, the air phase is close to the inner pipe wall. The highest air volume fraction (approximately 37%) can be observed close to the inner pipe wall, while the lowest air volume fraction (approximately 23%) can be observed close to the outer pipe wall. This may possibly results due to lift force action in small bubbles.

Additionally, the air volume fraction range for the annulus is around 23 to 37%, as indicated from the volume fraction profile. Furthermore, the air volume fraction which registers the highest point is found near the inner pipe wall for the air volume fraction profile.

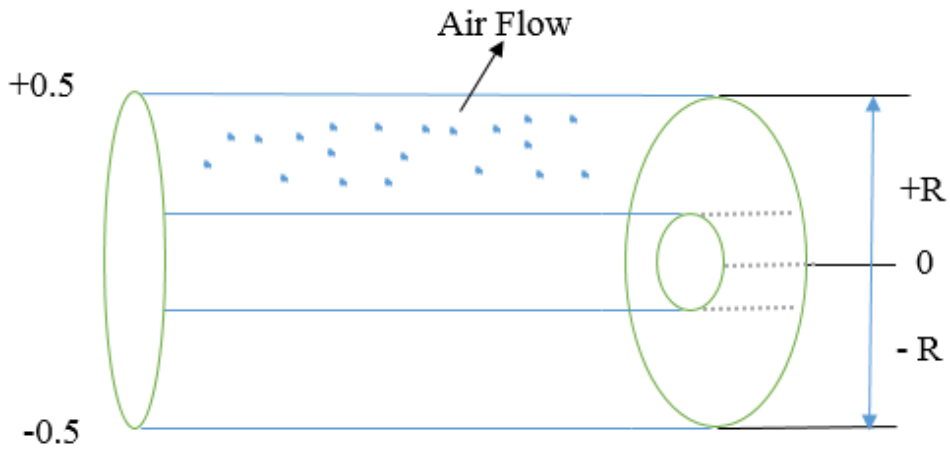

Figure 3-6 Concentric annular slug flow in horizontal annuli (A)

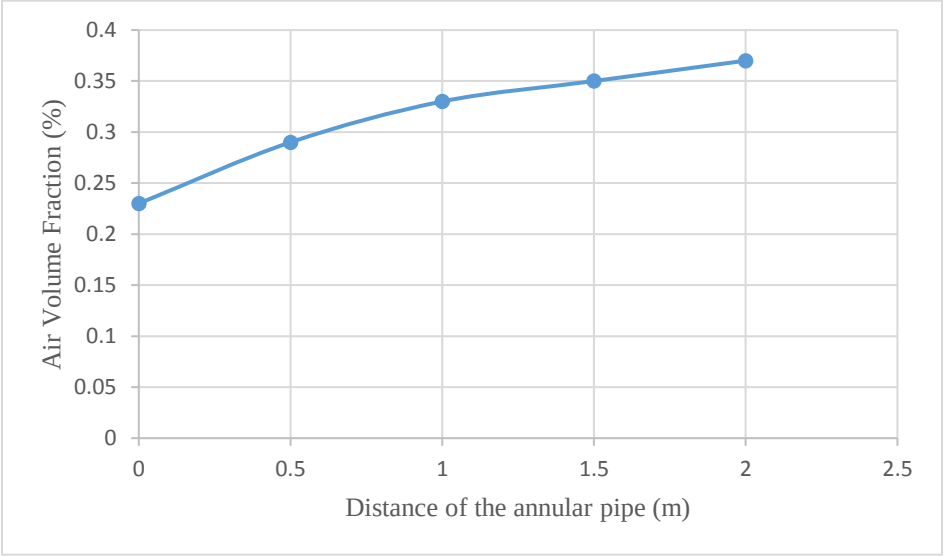

Figure 3-7 Concentric annular slug flow in horizontal annuli (B)

3.4.5 Sensitivity Analysis Comparison between slug flow volume fraction in pipeline and annular pipe

Table 3.1 Different liquid velocities with constant gas velocity used for simulation

Number	Gas superficial velocity(m/s)	Liquid superficial velocity(m/s)	Pipe type
1	0.4	0.3	Pipeline
2	0.4	0..3	Annular pipe

3.4.5.1 Slug flow volume fraction in pipeline

In the development phase of multiphase pipelines and related machinery, one of the most important parameters in both the slug body and gas void fraction is volume fraction. This is because, in designing the equipment, phase composition and volume fraction must be precisely proportional. Figure 3-8 shows simulation outcomes of a void fraction for an air-water slug flow regime situated by the cross-section of a horizontal pipe with length 2 m and dimeter 0.05 m. Figure 3-8 also illustrates air and water distribution for the horizontal slug flow, with dark blue indicating the air and red the water, both of which are separated by a line indicating their interface. In the simulation, water slugs reached as far as the top of the pipe for complete slug regime. The water phase, however, became unbalanced at the initial wave crest due to sinusoidal perturbation near the inlet. After that point, sizeable waves were noted, growing increasingly and taking up the entire cross-section at the pipe end. A lengthy slug could be seen increasing in size near the pipe downstream. Overall, as the gas superficial velocity increased.

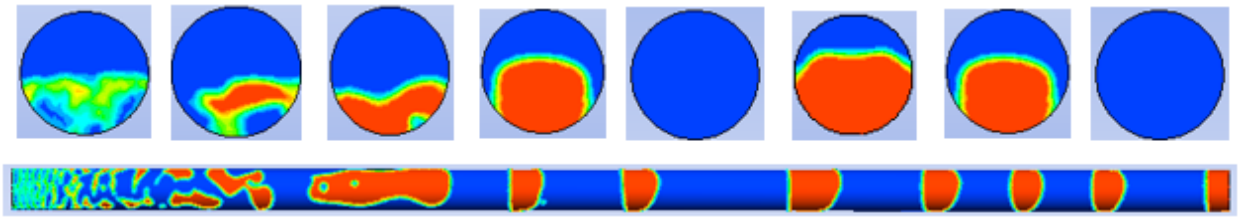

Figure 3-8 Sectional of liquid and gas volume fraction evaluation along the pipe length

3.4.5.2 Slug flow volume fraction in annular pipe

As presented in the contour plots, we successfully simulated the slug flow in horizontal annuli pipe with length of 2 m and outer diameter of 0.04, inure diameter of 0.02 m. Figure 3-9 shows simulation outcomes of a void fraction for an air-water slug flow, with dark blue indicating the air and red the water. From the contour plots, we can only visualize slug flow patterns. Figure 3-9 shows the slug portion of the slug unit as well as the accompanying bubble. As can be seen, the Slug size can only be estimated due to their continuous evolution and change. Figure 3-9 also shows the positioning of the slug bubbles as well as their distribution at the top and bottom of the annulus.

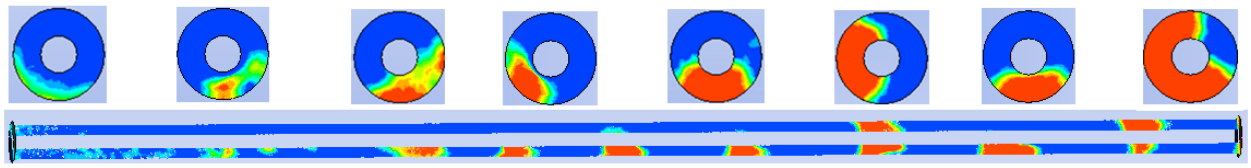

Figure 3-9 Sectional of liquid and gas volume fraction evaluation along the annular pipe length

3.4.5.3 Slug Flow Volume fraction Analysis with Time

Figure 3-10 and Figure 3-11 show water slugs breaching the upper portion in the pipeline as well as the annulus pipe, resulting in a complete slug regime. As can be seen, the upper portion is filled with air with the water slugs portion is filled. In fact, the water portion remains unsteady to the point of the first wave crest.

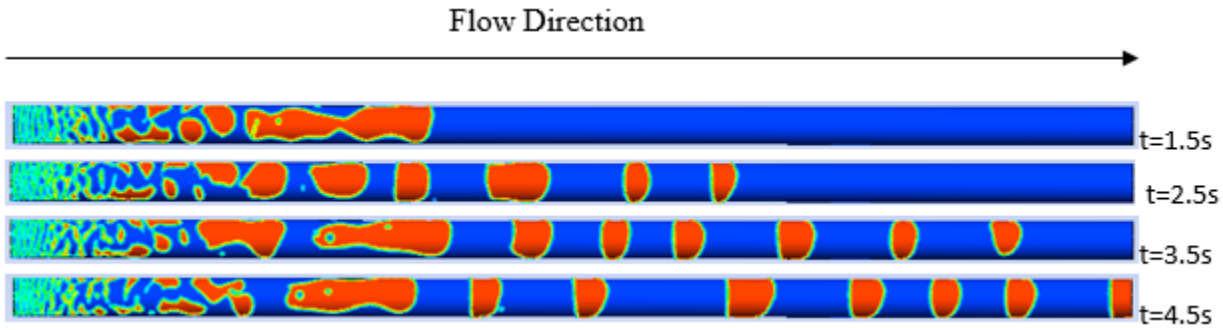

Figure 3-10 Slug flow trend at different time lapse indicating time in horizontal pipeline

This is due to sinusoidal perturbation of the inlet. Then, when large waves occurred, the pipe's cross-section begins to fill at 3.5s, while the annulus fills at 4.5s

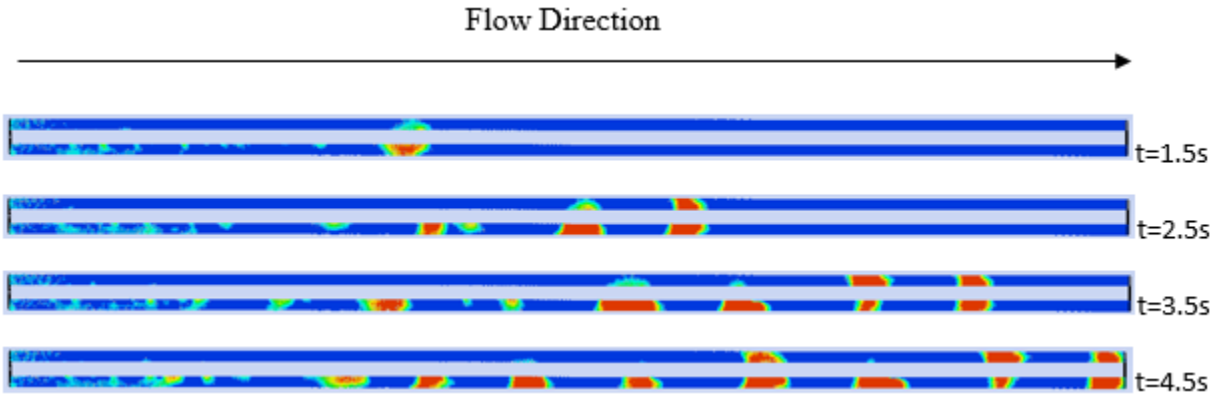

Figure 3-11 Slug flow trend at different time lapse indicating time in horizontal annular pipe

3.6 Conclusions

The outcome of the simulation tests clearly showed the ability of the CFD model to demonstrate the curvature effect resulting from annuli geometry. Because of the effect, the mean axial velocity profile of a completely turbulent flow within the concentric annuli manifested as asymmetrical and tilted in the direction of the inner wall. The form of the velocity profile was also impacted by the inner-to-outer radius ratio. This work attempted to illustrate the flow features of air-water flow within horizontal pipelines and annular pipe. CFD test simulations were performed with ANSYS FLUENT software. By applying the VOF approach slug was accurately predicted. As well, the outcomes of the simulation were validated against earlier experimental results and a reasonably good agreement was seen for the slug flow pattern. However, flow features; including velocity profile, pressure, and volume fraction, pertaining to annular and slug flow were investigated. These findings indicate that total pressure rises as water velocity increases in the annular pipe and pipeline slug flow, at the same time, the air volume fraction simulations present maximum value at the cross-section of along the length for both pipes. The outcomes reflect real flow configurations. Overall, the results from this work could prove helpful in the area of crude oil transportation, specifically in the development of pipeline infrastructure.

Chapter 4

Conclusions and Recommendations for Future Research Work

4.1 Conclusions

In the present study, CFD simulations were performed using ANSYS 16.2 FLUENT software. The application of the Eulerian model / Reynolds Stress Model (RSM) and the volume of fluid (VOF) model / Shear-Stress-Transport (SST) model not only showed good slug flow prediction capabilities but also validated experimental results. As shown, gas-liquid multi-phase slug flows are highly dependent on flow strength emanating from gas and liquid flow. However, flow strengths vary and fluctuate according to conditions. Given this situation, it was discovered that enhanced mesh discretization improved resolution and thus offered better overall outcomes. This study focused on the theoretical representation of slug flow in both horizontal and annular pipes. For this, a 3-D CFD / VOF model was employed to serve as the interface for the gas and liquid and for the tube's inner fluid flow. Because this theoretical model was shown to succeed at detecting flow regimes as well as gas volume fraction, CFD should be considered as a viable approach in predicting tube-based gas/liquid multi-phase flows.

Additionally, the research results could provide a basis for developing crude oil transport pipeline systems, as using CFD for modeling and flow assurance has been shown to improve the use of simulations. Hence, although CFD decreases the need for theoretical experimentation, it should not take the place of experimental analysis. The input data in CFD is often uncertain, prolonging both the validation and verification stages and having a negative impact on mathematical models. Thus, prior to applying CFD for modeling, researchers should first take into consideration the number of computations that will be required to give viable results.

4.2 Recommendations for Future Research Work

- Further analysis is required with more accuracy which can include choosing different coefficients and constants to minimize small errors and increase acceptancy of this model at versatile conditions of operation.
- It is expected to find out numerical correlations between different parameters by conducting further parametric study at distinct phases of fluid flow through pipeline and annuli.
- Complex geometry of pipeline and annuli can be introduced (e.g. bending, inclination etc.).
- Elaborate work on Fluid Structure Interaction (FSI) is required focusing the safety and risk at multiphase slug flow conditions through pipeline and annuli.

References

1. Meland, Knut Å. Stabilization of Two- Phase Flow in Risers from Reservoirs - Robust Anti-Slug Control Strategies. Edited by Sigurd Skogestad., NTNU, 2011.
2. Frank, Thomas. "Numerical simulation of slug flow regime for an air-water two-phase flow in horizontal pipes." Proceedings of the 11th International Topical Meeting on Nuclear Reactor Thermal-Hydraulics (NURETH-11), Avignon, France, October. 2005.
3. Crowe, Clayton T., John D. Schwarzkopf, Martin Sommerfeld, and Yutaka Tsuji. Multiphase flows with droplets and particles. CRC press, Taylor & Francis Group, Boca Raton, Florida 2011.
4. Van Wachem, B. G. M., and Alf-Erik Almstedt. "Methods for multiphase computational fluid dynamics." Chemical Engineering Journal 96.1 (2003): 81-98.
5. Stenmark, Elin "On multiphase flow models in ANSYS CFD software." Master thesis, Chalmers University of Technology, Sweden (2013).
6. Dewangan, S. K., & Sinha, S. L. (2016). Exploring the hole cleaning parameters of horizontal wellbore using two-phase Eulerian CFD approach. The Journal of Computational Multiphase Flows, 8(1), 15-39.
7. Soliman, R., & Collier, P. (1990). Pressure drop in slurry lines. Hydrocarbon Processing, 69(11), Hydrocarbon Processing, 1990, Vol.69 (11).
8. Roco, M. C., & Shook, C. A. (1983). Modeling of slurry flow: the effect of particle size. The Canadian Journal of Chemical Engineering, 61(4), 494-503.
9. Choi, Young-Chan, Park, Tae-Jun, Kim, Jae-Ho, Lee, Jae-Goo, Hong, Jae-Chang, & Kim, Yong-Goo. (2001). Experimental studies of 1 ton/day coal slurry feed type oxygen blown, entrained flow gasifier. Korean Journal of Chemical Engineering, 18(4), 493-498.

10. Huilin, Gidaspow, & Bouillard. (2002). Chaotic behavior of local temperature fluctuations in a laboratory-scale circulating fluidized bed. Powder Technology, 123(1), 59-68.
11. Brandstaetter, W., Ragab, A., & Shalaby, S. (2007). Modeling of Two-Phase Flow, and Slug Flow Characteristics in Horizontal/Inclined Pipelines using CFD. SPE Romanian Section Conference.
12. Frank, T. (2005, October). Numerical simulation of slug flow regime for an air-water two-phase flow in horizontal pipes. In Proceedings of the 11th International Topical Meeting on Nuclear Reactor Thermal-Hydraulics (NURETH-11), Avignon, France, October (pp. 2-6).
13. Al-Lababidi, S., Addali, A., Yeung, H., Mba, D., & Khan, F. (2009). Gas void fraction measurement in two-phase gas/liquid slug flow using acoustic emission technology. Journal of Vibration and Acoustics, 131(6), 064501.
14. Czapp, M., Utschick, M., Rutzmoser, J., & Sattelmayer, T. (2012, July). Investigations on slug flow in a horizontal pipe using stereoscopic particle image velocimetry and CFD simulation with volume of fluid method. In 2012 20th International Conference on Nuclear Engineering and the ASME 2012 Power Conference (pp. 477-486). American Society of Mechanical Engineers.
15. Razavi, S. Y., & Namin, M. M. (2011). Numerical model of slug development on horizontal two-phase flow. In Proceedings of the International Conference on Recent Trends in Transportation, Environmental and Civil Engineering (pp. 14-15).
16. Al-Hashimy, Z. I., Al-Kayiem, H. H., Time, R. W., & Kadhim, Z. K. (2016). Numerical Characterisation of Slug Flow in Horizontal Air/water Pipe Flow. International Journal of Computational Methods and Experimental Measurements, 4(2), 114-130.

17. Taitel, Y., & Dukler, A. E. (1976). A model for predicting flow regime transitions in horizontal and near horizontal gas-liquid flow. AIChE Journal, 22(1), 47-55.
18. Ghorai, S., & Nigam, K. D. P. (2006). CFD modeling of flow profiles and interfacial phenomena in two-phase flow in pipes. Chemical Engineering and Processing: Process Intensification, 45(1), 55-65.
19. Tan ping, FU xingjun et al. Study on Vibration of Conveying Water Piping System in Power Plant, Turbine Technology, Vol .46, No.2, 2004.
20. Chica, L., Pascali, R., Jukes, P., Ozturk, B., Gamino, M., & Smith, K. (2012, July). Detailed FSI Analysis Methodology for Subsea Piping Components. In ASME 2012 31st International Conference on Ocean, Offshore and Arctic Engineering (pp. 829-839). American Society of Mechanical Engineers.
21. Anderson, T. B., & Jackson, R. (1967). Fluid mechanical description of fluidized beds. Equations of
22. Bowen, R. M. (1976). Theory of mixtures. Continuum physics, 3(Pt I)
23. Alder, B. J., & Wainwright, T. E. (1960). Studies in molecular dynamics. II. Behavior of a small number of elastic spheres. The Journal of Chemical Physics, 33(5), 1439-1451.
24. Chorin, A. J. (1968). Numerical solution of the Navier-Stokes equations. Mathematics of computation, 22(104), 745-762.
25. Launder, B. E. (1989). Second-moment closure and its use in modelling turbulent industrial flows. International Journal for Numerical Methods in Fluids, 9(8), 963-985.
26. Chica, L. (2014). FSI study of internal multiphase flow in subsea piping components (Doctoral dissertation, University of Houston).

27. Nouri, J. M., Umur, H., & Whitelaw, J. H. (1993). Flow of Newtonian and non-Newtonian fluids in concentric and eccentric annuli. Journal of Fluid Mechanics, 253, 617-641.
28. Chung, S. Y., Rhee, G. H., & Sung, H. J. (2001). Direct Numerical Simulation of Turbulent Concentric Annular Pipe Flow. In TSFP Digital Library Online. Begel House Inc.
29. Al-Hashimy, Z. I., Al-Kayiem, H. H., Kadhim, Z. K., & Mohmmed, A. O. (2015). Numerical simulation and pressure drop prediction of slug flow in oil/gas pipelines. Computational Methods in Multiphase Flow VIII, 89, 57.
30. Kristiansen, O. (2004). Experiments on the transition from stratified to slug flow in multiphase pipe flow. PhD thesis, Norwegian University of Science and Technology (NTNU) Trondheim.
31. Orell, A. (2005). Experimental validation of a simple model for gas–liquid slug flow in horizontal pipes. Chemical Engineering Science, 60(5), 1371-1381.
32. Jepson, W. P., & Taylor, R. E. (1993). Slug flow and its transitions in large-diameter horizontal pipes. International journal of multiphase flow, 19(3), 411-420.
33. Ghorai, S., & Nigam, K. D. P. (2006). CFD modeling of flow profiles and interfacial phenomena in two-phase flow in pipes. Chemical Engineering and Processing: Process Intensification, 45(1), 55-65.
34. Thome, J. R. (2004). Engineering data book III. Wolverine Tube Inc, 2010.
35. De Henau, V., & Raithby, G. D. (1995). A transient two-fluid model for the simulation of slug flow in pipelines—I. Theory. International Journal of Multiphase Flow, 21(3), 335-349.
36. Ghosh, S., Das, G., & Das, P. K. (2010). Simulation of core annular down flow through CFD—A comprehensive study. Chemical Engineering and Processing: Process Intensification, 49(11), 1222-1228.

37. Kaushik, V. V. R., Ghosh, S., Das, G., & Das, P. K. (2012). CFD simulation of core annular flow through sudden contraction and expansion. Journal of Petroleum Science and Engineering, 86, 153-164.
38. Ghosh, S., Das, G., & Das, P. K. (2011). Simulation of core annular in return bends—a comprehensive CFD study. Chemical Engineering Research and Design, 89(11), 2244-2253.
39. Fluent, A. N. S. Y. S. "Ansys Fluent Theory Guide." ANSYS Inc., USA (2011).
40. Wen, J. X., Le Fur, P., Jie, H., & Vendra, C. M. R. (2016). Further development and validation of Co_2 FOAM for the atmospheric dispersion of accidental releases from carbon dioxide pipelines. International Journal of Greenhouse Gas Control, 52, 293-304
41. Alder, B. J., & Wainwright, T. E. (1960). Studies in molecular dynamics. II. Behavior of a small number of elastic spheres. The Journal of Chemical Physics, 33(5), 1439-1451.
42. Anderson, T. B., & Jackson, R. (1967). Fluid mechanical description of fluidized beds. Equations of motion. Industrial & Engineering Chemistry Fundamentals, 6(4), 527-539.
43. Menter, F. R. (1994). Two-equation eddy-viscosity turbulence models for engineering applications. AIAA journal, 32(8), 1598-1605.
44. Wilcox, D. C. (1998). Turbulence modeling for CFD (Vol. 2, pp. 103-217). La Canada, CA: DCW industries
45. Walters, D. K., & Cokljat, D. (2008). A three-equation eddy-viscosity model for Reynolds-averaged Navier–Stokes simulations of transitional flow. Journal of fluids engineering, 130(12), 121-401.
46. Ozbayoglu, M. E., & Omurlu, C. (2007). Modelling of two-phase flow through concentric annuli. Petroleum science and technology, 25(8), 1027-1040.

47. Nouri, J. M., & Whitelaw, J. H. (1994). Flow of Newtonian and non-Newtonian fluids in a concentric annulus with rotation of the inner cylinder. Transactions-American Society of Mechanical Engineers Journal of Fluids Engineering, 116, 821-821.

48. Lewis, S., Fu, W. L., & Kojasoy, G. (2002). Internal flow structure description of slug flow-pattern in a horizontal pipe. International journal of heat and mass transfer, 45(19), 3897-3910.

49. H. Hadia, R. A. Sultan, M. A. Rahman, J. Shirokoff, S. Zendehboudi, A Computational Fluid Dynamics Study of Two-Phase Slurry and Slug Flow in Horizontal Pipelines, 3rd Workshop and Symposium on Safety and Integrity Management of Operations in Harsh Environments (C-RISE3).

50. H. Hadia, J. Shirokoff, M.A. Rahman, R. A. Sultan, S. Zendehboudi, Analysis of Two Phase Slug Flow through Annular Pipeline, Qatar Conference on CFD, (2017).

51. I. A. Adeoti, R. A Sultan H. Hadia, M. A. Rahman, J. Shirokoff, A. Maynard, and M. Addy, CFD Approach to Analyze Slug Flow Induced Fluid Structure Interaction (FSI) through Pipeline and Annuli, Journal of Computational Science (2017) submitted.